Differential adhesion regulates neurite placement via a retrograde zippering mechanism

Authors: Titas Sengupta[1], Noelle L. Koonce[1], Mark W. Moyle[1], Leighton H. Duncan[1], Nabor Vázquez-Martínez[1], Sarah E. Emerson[1], Xiaofei Han[2], Lin Shao[1], Yicong Wu[2], Anthony Santella[3], Li Fan[3], Zhirong Bao[3], William A. Mohler[5], Hari Shroff[2, 4], Daniel A. Colón-Ramos[1, 4, 6,*]

Affiliations:

1. Department of Neuroscience and Department of Cell Biology, Yale University School of Medicine, New Haven, CT 06536, USA.

2. Laboratory of High Resolution Optical Imaging, National Institute of Biomedical Imaging and Bioengineering, National Institutes of Health, Bethesda, MD 20892, USA.

3. Developmental Biology Program, Sloan Kettering Institute, New York, NY 10065, USA.

4. MBL Fellows, Marine Biological Laboratory, Woods Hole, MA 02543, USA

5. Department of Genetics and Genome Sciences and Center for Cell Analysis and Modeling, University of Connecticut Health Center, Farmington, CT 06030, USA.

6. Instituto de Neurobiología, Recinto de Ciencias Médicas, Universidad de Puerto Rico, San Juan 00901, Puerto Rico.

*Correspondence to:

Daniel A. Colón-Ramos, Ph.D.
Department of Neuroscience
Department of Cell Biology
Yale University School of Medicine
333 Cedar Street
SHM B 163D
New Haven, CT 06510
Email: daniel.colon-ramos@yale.edu

Abstract

During development, neurites and synapses segregate into specific neighborhoods or layers within nerve bundles. The developmental programs guiding placement of neurites in specific layers, and hence their incorporation into specific circuits, are not well understood. We implement novel imaging methods and quantitative models to document the embryonic development of the *C. elegans* brain neuropil, and discover that differential adhesion mechanisms control precise placement of single neurites onto specific layers. Differential adhesion is orchestrated via developmentally-regulated expression of the IgCAM SYG-1, and its partner ligand SYG-2. Changes in SYG-1 expression across neuropil layers result in changes in adhesive forces, which sort SYG-2-expressing neurons. Sorting to layers occurs, not via outgrowth from the neurite tip, but via an alternate mechanism of retrograde zippering, involving interactions between neurite shafts. Our study indicates that biophysical principles from differential adhesion govern neurite placement and synaptic specificity *in vivo* in developing neuropil bundles.

Introduction

In brains, neuronal processes or neurites are segregated away from cell bodies into synapse-rich regions termed neuropils: dense structures of nerve cell extensions which commingle to form functional circuits (Maynard, 1962). In both vertebrates and invertebrates, placement of neurites into specific neighborhoods results in a laminar organization of the neuropil (Kolodkin and Hiesinger, 2017, Millard and Pecot, 2018, Nevin et al., 2008, Sanes and Zipursky, 2010, Schürmann, 2016, Soiza-Reilly and Commons, 2014, Xu et al., 2020, Zheng et al., 2018). The laminar organization segregates specific information streams within co-located circuits and is a major determinant of synaptic specificity and circuit connectivity (Baier, 2013, Gabriel et al., 2012, Missaire and Hindges, 2015, Moyle et al., 2021, Nguyen-Ba-Charvet and Chedotal, 2014, White et al., 1986, Xie et al., 2017). The developmental programs guiding placement of neurites along specific layers, and therefore circuit architecture within neuropils, are not well understood.

The precise placement of neurites within layered structures cannot be exclusively explained by canonical tip-directed outgrowth dynamics seen during developmental axon guidance (Tessier-Lavigne and Goodman, 1996). Instead, ordered placement of neurites resulting in layered patterns appears to occur via local cell-cell recognition events. These local cell-cell recognition events are modulated by the regulated expression of specific cell adhesion molecules (CAMs) that place neurites, and synapses, onto layers (Aurelio et al., 2003, Kim and Emmons, 2017, Lin et al., 1994, Petrovic and Hummel, 2008, Poskanzer et al., 2003, Schwabe et al., 2019). For example, studies in both the mouse and fly visual systems have revealed important

roles for the regulated spatio-temporal expression of IgSF proteins, such as Sidekick, Dscam and Contactin, in targeting synaptic partner neurons to distinct layers or sublayers (Duan et al., 2014, Sanes and Zipursky, 2010, Tan et al., 2015, Yamagata and Sanes, 2008, Yamagata and Sanes, 2012). In *C. elegans* nerve bundles, neurite position is established and maintained via combinatorial, cell-specific expression of CAMs which mediate local neurite interactions and, when altered, lead to reproducible defects in neurite order within bundles (Kim and Emmons, 2017, Yip and Heiman, 2018). How these local, CAM-mediated interactions are regulated during development and how they result in the segregation of neurites into distinct layers, are not well understood.

Differential expression of cell adhesion molecules (CAMs) in cells from early embryos can drive their compartmentalization (Foty and Steinberg, 2005, Foty and Steinberg, 2013, Steinberg, 1962, Steinberg, 1963, Steinberg, 1970, Steinberg and Takeichi, 1994). This compartmentalization is in part regulated by biophysical principles of cell adhesion and surface tension which can give rise to tissue-level patterns and boundaries (Canty et al., 2017, Duguay et al., 2003, Erzberger et al., 2020, Foty et al., 1996, Schotz et al., 2008). For example, morphogenic developmental processes such as the patterning of the *Drosophila* germline and retina, the germ layer organization in zebrafish, and the sorting of motor neuron cell bodies into discrete nuclei in the ventral spinal cord can be largely explained via differential adhesion mechanisms and cortical contraction forces that contribute to cell sorting (Bao and Cagan, 2005, Bao et al., 2010, Godt and Tepass, 1998, Gonzalez-Reyes and St Johnston, 1998, Krieg et al., 2008, Price et al., 2002, Schotz et al., 2008). While differential adhesion is best understood in

105 the context of the sorting of cell bodies in early embryogenesis, recent
106 neurodevelopmental work supports that this mechanism influences sorting of neuronal
107 processes *in vivo* as well. For example, differential expression of N-cadherin in the
108 *Drosophila* visual system underlies the organization of synaptic-partnered neurites
109 (Schwabe et al., 2019), where changes in the relative levels of N-cadherin are sufficient
110 to determine placement of neurites within nerve bundles. Whether differential adhesion
111 acts as an organizational principle within layered neuropils to regulate precise
112 placement of neurites is not known.

113 Here we examine the developmental events that lead to placement of the AIB
114 interneurons in the *C. elegans* nerve ring. The *C. elegans* nerve ring is a layered
115 neuropil, with specific strata functionally segregating sensory information and motor
116 outputs (Brittin et al., 2021, Moyle et al., 2021, White et al., 1986). A highly
117 interconnected group of neurons referred to as the 'rich club' neurons, and which
118 include interneuron AIB, functionally link distinct strata via precise placement of their
119 neurites (Moyle et al., 2021, Sabrin et al., 2019, Towlson et al., 2013). Each AIB
120 interneuron projects a single neurite, but segments of that single neurite are placed
121 along distinct and specific layers in the *C. elegans* nerve ring (Fig. 1). The sequence of
122 events resulting in the precise placement of AIB along defined nerve ring layers is
123 unexplored, primarily owing to limitations in visualizing these events *in vivo* during
124 embryonic stages.

125 We implemented novel imaging methods and deep learning approaches to yield
126 high-resolution images of AIB during embryonic development. We discovered that
127 placement of the AIB neurite depends on coordinated retrograde zippering mechanisms

that align segments of the AIB neurite onto specific neuropil layers. Quantitative analysis and modeling of our *in vivo* imaging data revealed that biophysical principles of differential adhesion influence the observed retrograde zippering mechanisms that result in the sorting of the AIB neurite shaft onto distinct neuropil strata. We performed genetic screens to identify the molecular mechanisms underpinning these differential adhesion mechanisms, discovering a role for the IgCAM receptor *syg-1* and its ligand, *syg-2*. We determined that *syg-2* acts in AIB to instruct neurite placement across strata, while *syg-1* is required non-cell autonomously, and at specific layers. Temporally-regulated expression of SYG-1 alters adhesive forces during development to sort segments of AIB onto specific layers. Ectopic expression of SYG-1 predictably affects differential adhesion across layers, repositioning the AIB neurite segments in a SYG-2-dependent manner. Our findings indicate that conserved principles of differential adhesion drive placement of neurites, and *en passant* synaptic specificity, in layered neuropils.

Results

Examination of AIB neurite architecture in the context of the nerve ring strata

First, we characterized the precise placement and synaptic distribution of the AIB neurite within the nerve ring neuropil strata. From electron microscopy connectome datasets and *in-vivo* imaging, we observed that the AIB neurite is unipolar, with its

single neurite placed along two distinct and specific strata of the nerve ring (Fig. 1, Supplementary Movies 1-3).

Connectomic studies have identified AIB as a “rich club” neuron, a connector hub that links nodes in different functional modules of the brain (Sabrin et al., 2019, Towlson et al., 2013). We observed that AIB’s role as a connector hub was reflected in its architecture within the context of the layered nerve ring (Fig. 1K-N, Supplementary Fig. 1, Supplementary Fig. 2). For example, the AIB neurite segment in the posterior neighborhood is enriched in postsynaptic specializations, enabling it to receive sensory information from the adjacent sensory neurons that reside in that neighborhood (Supplementary Fig. 2; (White et al., 1983, White et al., 1986)). AIB relays this sensory information onto the anterior neighborhood, where the AIB neurite elaborates presynaptic specializations that innervate neighboring motor interneurons (Fig. 1D, E, I, J; Supplementary Fig. 2A-G, Supplementary Movie 5). The architecture of AIB is reminiscent of that of amacrine cells of the inner plexiform layer (Demb and Singer, 2012, Kolb, 1995, Kunzevitzky et al., 2013, Robles et al., 2013, Strettoi et al., 1992, Taylor and Smith, 2012), which serve as hubs by distributing their neurites and synapses across distinct and specific sublaminae of the vertebrate retina (Marc et al., 2014). We set out to examine how this architecture was laid out during development.

A retrograde zippering mechanism positions the AIB neurites in the anterior neighborhood during embryonic development

Prior to this study, using characterized cell-specific promoters, AIB could be visualized in larvae (Altun et al., 2008, Kuramochi and Doi, 2019) but not in embryos,

when placement of AIB into the neighborhoods is specified (Supplementary Fig. 2A shows that by earliest postembryonic stage, L1, AIB neurite placement is complete, indicating placement occurs in the embryo). Moreover, continuous imaging of neurodevelopmental events in embryos, necessary for documenting AIB development, presents unique challenges regarding phototoxicity, speeds of image acquisition as it relates to embryonic movement, and the spatial resolution necessary to discern multiple closely-spaced neurites in the embryonic nerve ring (Wu et al., 2011). These barriers prevented documentation of AIB neurodevelopmental dynamics. To address these challenges, we first adapted a subtractive labeling strategy for sparse labeling and tracking of the AIB neurites in embryos (detailed in Methods, Supplementary Fig. 3A-C, Supplementary Movie 6, (Armenti et al., 2014)). We then adapted use of novel imaging methods, including dual-view light-sheet microscopy (diSPIM) (Kumar et al., 2014, Wu et al., 2013) for long-term isotropic imaging, and a triple-view line-scanning confocal imaging and deep-learning framework for enhanced resolution (Supplementary Fig. 3D,E; (Weigert et al., 2018, Wu et al., 2016); Wu et al., in prep).

Using these methods, we observed that the AIB neurites enter the nerve ring during the early embryonic elongation phase, ~400 minutes post fertilization (m.p.f). The two AIB neurites then circumnavigate the nerve ring at opposite sides of the neuropil - both AIBL and AIBR project dorsally along the posterior neighborhood, on the left and right-hand sides of the worm, respectively (Fig. 2A,B). Simultaneous outgrowth of AIBL and AIBR neurons in the posterior neighborhood results in their neurites circumnavigating the ring and meeting at the dorsal midline of the nerve ring (Fig. 2C).

Therefore, proper placement of the proximal segment of the AIB neurite in the posterior neighborhood occurs by AIB outgrowth along neurons in this neighborhood (Fig. 2A-F).

After meeting at the dorsal midline, instead of making a shift to the anterior neighborhood (as expected from the adult AIB neurite morphology – see Fig. 1M,N), the AIB neurites, surprisingly, continue growing along the posterior neighborhood (Fig. 2C,D; 480 m.p.f.). At approximately 505 m.p.f., each AIB neurite separates from the posterior neighborhood, starting at its growth cone, by growing tangentially to the posterior neighborhood (the posterior neighborhood is marked in Fig. 2A-G by its lateral counterpart, i.e., the other AIB, also see Supplementary Fig. 3I,J). The departure of the AIB growth cone occurs due to the AIB neurite growing in a straight path trajectory instead of following the bending nerve ring arc (Supplementary Fig. 3I,J). Because it has been documented that axons tend to 'grow straight' on surfaces lacking adhesive forces that instruct turning (Katz, 1985), we hypothesize that the observed exit (via 'straight outgrowth') could result from decreased adhesion to the posterior neighborhood (Supplementary Fig. 3I,J).

As it grows tangentially to the posterior neighborhood, the AIB neurite cuts orthogonally through the nerve ring and towards the anterior neighborhood (Supplementary Fig. 3I,J). Upon intersecting the anterior neighborhood, the AIB neurite reengages with the arc of the nerve ring. At this developmental stage (Fig 2I), only 3.9% of the AIB distal neurite is placed in the anterior neighborhood, with the remainder still being positioned in the posterior neighborhood and between neighborhoods. Following this, we observed a repositioning of the AIB neurite, but not via expected tip-directed fasciculation. Instead, the entire shaft of the distal AIB neurite was peeled away from

the posterior neighborhood and repositioned onto the anterior neighborhood, starting from the tip of the neurite and progressively 'zippering' in a retrograde fashion towards the cell body (Fig. 2J,K; the overlap of the AIB neurite with the anterior neighborhood increased from 3.9% at 515 m.p.f. to 30.4% at 530 m.p.f. and 71.7% at 545 m.p.f.). Retrograde zippering stopped at the dorsal midline of the nerve ring (~545 m.p.f.), resulting in the AIB architecture observed in postembryonic larval and adult stages (Fig. 2L). The progressive zippering of the AIB neurite onto the anterior neighborhood occurs concurrently with its separation from the posterior neighborhood (Fig. 2M), a converse process which we refer to as 'unzippering'. The *in vivo* developmental dynamics of AIB repositioning, via retrograde zippering onto the anterior neighborhood, are reminiscent of dynamics observed in cultures of vertebrate neurons in which biophysical forces drive 'zippering' of neurite shafts, and the bundling of neurons (Smit et al., 2017).

Biophysical modeling of AIB developmental dynamics is consistent with differential adhesion leading to retrograde zippering

Dynamics of neurite shaft zippering have been previously documented (Barry et al., 2010, Voyiadjis et al., 2011) and modeled in tissue culture cells (Smit et al., 2017), and described as resulting from two main forces: neurite-neurite adhesion (represented as "S") and mechanical tension (represented as "T"). To better understand the underlying mechanisms of AIB neurite placement, we analyzed AIB developmental dynamics in the context of these known forces that affect neurite zippering. In each neighborhood, the developing AIB neurite experiences two forces: (i) adhesion to neurons in that neighborhood and (ii) tension due to mechanical stretch. As the neurite

zippers and unzippers, it has a velocity in the anterior neighborhood (a zippering velocity, v_{zip}) and a velocity in the posterior neighborhood (an unzippering velocity, v_{unzip}) (Fig. 3 and Supplementary Note). These velocities are related to the forces on the neurite by the following equation:

$$v_{zip} + v_{unzip} = \frac{(S_{anterior} - S_{posterior})}{\eta} - \frac{\Delta T}{\eta}(1 - cos\theta)$$

where v_{zip} = zippering velocity, v_{unzip} = unzippering velocity, $S_{anterior} - S_{posterior}$ = difference between adhesive forces in the two neighborhoods, $\Delta T = T_{anterior} - T_{posterior}$ = difference between tension acting on the AIB neurite in the two neighborhoods, η = friction constant (see Supplementary Note) and θ = angle of the AIB neurite to the neighborhoods (Fig. 3 and Supplementary Note). Since the above biophysical equation defines the relationship between velocities and forces, we measured the velocities of the neurite from our time-lapse images to make predictions about the forces on the neurite.

Time lapse images and measurements of the developmental dynamics showed that zippering and unzippering takes place concurrently: zippering on to the anterior neighborhood and unzippering from the posterior one (Fig. 3C). Between 505-545 m.p.f., the average length of the AIB neurite that is placed in the anterior neighborhood (4.49 μm) by retrograde zippering is similar to the length that is unzippered from the posterior neighborhood (4.13 μm). Assuming, based on previous studies (Smit et al., 2017), that the tension forces are uniformly distributed along the neurite (and therefore

263 $\Delta T = T_{anterior} - T_{posterior} = 0$), zippering and unzippering velocities arise from a
264 difference in adhesion ($S_{anterior} - S_{posterior} > 0$) (see Supplementary Note).

265 Measurements of *in vivo* zippering velocities (Fig. 3D) support this hypothesis.
266 Examination of our time-lapse images revealed that AIB neurite zippering onto the distal
267 neighborhood takes place at higher velocities at later timepoints (with mean zippering
268 velocity increasing from 0.09 μm/min at 515 mins to 0.34 μm/min at 530 mins) (Fig. 3D).
269 This increased velocity, or acceleration, is a hallmark of force imbalance and consistent
270 with a net increase in adhesive forces in the anterior neighborhood during the period in
271 which zippering takes place. We note that retrograde zippering comes to a stop
272 precisely at the dorsal midline, likely owing to the adhesion and tension forces on the
273 neurite in the two neighborhoods balancing out at this point. Together, the
274 developmental dynamics observed for AIB neurite placement are consistent with
275 relative changes in adhesive forces between the neighborhoods. This suggests that
276 dynamic mechanisms resulting in differential adhesion might govern AIB neurite
277 repositioning.

278

279 **SYG-1 and SYG-2 regulate precise placement of the AIB neurite to the**
280 **anterior neighborhood**

281 To identify the molecular mechanism underpinning differential adhesion for AIB
282 neurodevelopment, we performed forward and reverse genetic screens. We discovered
283 that loss-of-function mutant alleles of *syg-1* and *syg-2*, which encode a pair of
284 interacting Ig family cell adhesion molecules (IgCAMs), display significant defects in the
285 placement of the AIB neurite. In wild type animals, we reproducibly observed complete

overlap between the AIB distal neurite and neurons in the anterior neighborhood (Fig. 4A-D), consistent with EM characterizations (Supplementary Fig. 2A,B). In contrast, 76.3% of *syg-1(ky652)* animals and 60% of *syg-2(ky671)* animals (compared to 1.8% of wild type animals) showed regions of AIB detachment from neurons specifically in the anterior neighborhood (Fig. 4E-L; we note we did not detect defects in general morphology of the nerve ring, in the length of the AIB distal neurite, or in position of the AIB neurite in the posterior neighborhood for these mutants, Supplementary Fig. 4). In the *syg-1(ky652)* and *syg-2(ky671)* animals that exhibit defects in AIB neurite placement, we found that 21.49±4.0% and 17.33±3.9% (respectively) of the neurite segment in the anterior neighborhood is detached from the neighborhood (Fig. 4M). Our findings indicate that SYG-1 and SYG-2 are required for correct placement of AIB, specifically to the anterior neighborhood.

The IgCAMs SYG-1 and SYG-2 are a receptor-ligand pair that has been best characterized in the context of regulation of synaptogenesis in the *C. elegans* egg-laying circuit (Shen and Bargmann, 2003, Shen et al., 2004). SYG-1 (Rst and Kirre in *Drosophila* and Kirrel1/2/3 in mammals) and SYG-2 (Sns and Hibris in Drosophila, and Nephrin in mammals) orthologs also act as multipurpose adhesion molecules in varying conserved developmental contexts (Bao and Cagan, 2005, Bao et al., 2010, Chao and Shen, 2008, Garg et al., 2007, Neumann-Haefelin et al., 2010, Ozkan et al., 2014, Oztokatli et al., 2012, Serizawa et al., 2006, Shen and Bargmann, 2003, Shen et al., 2004, Strunkelnberg et al., 2001). In most of the characterized *in vivo* contexts, SYG-1 has been shown to act heterophilically with SYG-2 (Dworak et al., 2001, Ozkan et al., 2014, Shen et al., 2004). Consistent with SYG-1 and SYG-2 acting jointly for precise

placement of the AIB neurite *in vivo*, we observed that a double mutant of the *syg-1(ky652)* and *syg-2 (ky671)* loss-of-function alleles did not enhance the AIB distal neurite placement defects as compared to either single mutant (Fig. 4N).

To determine the site of action of these two molecules, we expressed them cell-specifically in varying tissues. We observed that SYG-2 expression in AIB was sufficient to rescue the AIB distal neurite placement defects in the *syg-2(ky671)* mutants, suggesting that SYG-2 acts cell autonomously in AIB. While expression of wild-type SYG-1 (via a cosmid) rescued AIB neurite placement onto the anterior neighborhood, expression of SYG-1 using an AIB cell-specific promoter did not (Fig. 4N), consistent with SYG-1 regulating AIB neurite placement cell non-autonomously.

Increased local expression of SYG-1 in the anterior neighborhood coincides with zippering of the AIB neurite onto this neighborhood

To understand how SYG-1 coordinates placement of the AIB neurite, we examined the expression of transcriptional and translational reporters of SYG-1 in the nerve ring of wild type animals. In postembryonic, larva-stage animals (L3 and L4), we observed robust expression of the *syg-1* transcriptional reporter in a banded pattern in ~20 neurons present in the AIB posterior and anterior neighborhoods, with specific enrichment in the anterior neighborhood (Fig. 5A-E). The SYG-1 translational reporter, which allowed us to look at SYG-1 protein accumulation, also showed a similar expression pattern (Fig. 5F-I). To understand how SYG-1 regulates placement of the AIB neurite during development, we examined spatiotemporal dynamics of expression

of SYG-1 during embryogenesis at the time of AIB neurite placement (400-550 m.p.f.) (Fig. 2), using both the transcriptional and translational *syg-1* reporters.

Prior to 470 m.p.f., *syg-1* reporter expression in the nerve ring was primarily restricted to a single band corresponding to the AIB posterior neighborhood (Fig. 5K,O,O'). This coincides with periods of outgrowth and placement of the AIB neurons in the posterior neighborhood. However, over the subsequent three hours of embryogenesis (470-650 m.p.f.), SYG-1 expression levels progressively increase in the anterior neighborhood while decreasing in the posterior neighborhood (Fig. 5L-R', Supplementary Fig. 5, Supplementary Movie 7). The change in expression levels of SYG-1 across neighborhoods coincides with the relocation of the AIB neurite, from the posterior to the anterior neighborhood via retrograde zippering (Fig. 5S). Our observations *in vivo* are consistent with reported SYG-1 expression levels from embryonic transcriptomics data (Packer et al., 2019), which demonstrate similar SYG-1 expression changes in neurons in the anterior and posterior neighborhoods of AIB (Supplementary Table 1). The transcriptomic studies also demonstrate a ten-fold increase in SYG-2 transcript levels in AIB at the time in which the AIB neurite transitions between neighborhoods (and consistent with our findings that SYG-2 acts cell autonomously in AIB). Together with the biophysical analyses, our data suggests that spatiotemporal changes in SYG-1 and SYG-2 expression might result in changes in forces that drive differential adhesion of AIB neurites via retrograde zippering of their axon shafts.

Ectopic *syg-1* expression is sufficient to alter placement of the AIB distal neurite

To test whether coincident SYG-1 expression in the anterior neighborhood was responsible for repositioning of AIB to that neighborhood, we set to identify and manipulate the sources of SYG-1 expression. We found that increases of SYG-1 in the anterior neighborhood were caused by (i) ingrowth of SYG-1-expressing neurons into the anterior neighborhood and (ii) onset of *syg-1* expression in neurons of the anterior neighborhood (Supplementary Fig. 5). We observed strong and robust SYG-1 expression in the RIM neurons, the primary postsynaptic partner of AIB, both in embryonic and postembryonic stages, leading us to hypothesize that SYG-1 expression in RIM neurons contributes to AIB neurite placement (Supplementary Fig. 6). To test this hypothesis, we ablated RIM neurons. We observed that RIM ablations result in defects in AIB neurite placement which phenocopied those seen for *syg-1* loss-of-function mutants (Supplementary Fig. 7). We also observed that expression of SYG-1 specifically in RIM and RIC neurons in *syg-1(ky652)* mutants was sufficient to position the AIB distal neurite along these neurons (Supplementary Fig. 7P-Q').

If differences in SYG-1 expression level between the neighborhoods results in differential adhesion, and consequent relocation of the AIB distal neurite from the posterior to the anterior neighborhood, then purposefully altering these differences should predictably alter the position of the AIB neurite. We aimed to test this hypothesis by inverting the adhesion differential through the overexpression of SYG-1 in the posterior neighborhood (see Methods). Unlike wild type and *syg-1* mutants (Fig. 6A-F, Supplementary Fig. 8A,B), animals with ectopic *syg-1* expression in the posterior

neighborhood displayed a gain-of-function phenotype, in which the AIB distal neurite remained partially positioned in the posterior neighborhood throughout postembryonic larval stages (Fig. 6G-J, Supplementary Fig. 8A,B). Importantly, these gain-of-function effects caused by ectopic expression of SYG-1 are not observed in a *syg-2(ky671)* mutant background, consistent with SYG-2 expression in AIB being required for AIB's repositioning to the SYG-1 expressing layers. Our findings indicate that inverting the adhesion differential via enrichment of SYG-1 in the 'wrong' neighborhood predictably affects relocation of the AIB distal neurite in a way that is consistent with differential adhesion mechanisms.

We reasoned that if differential adhesion mechanisms were driving zippering of the AIB neurite during development, expression of the SYG-1 ectodomain would be sufficient to drive the ectopic interactions upon misexpression (Chao and Shen, 2008, Galletta et al., 2004, Gerke et al., 2003). Indeed, expression of the SYG-1 ectodomain in the posterior neighborhood resulted in gain-of-function phenotypes for AIB neurite placement, similar to those seen with misexpression of full-length SYG-1 (although penetrance of these effects was lower than that observed with full-length SYG-1). Consistent with the importance of adhesion-based mechanisms in the observed phenotypes, ectopic expression of the SYG-1 endodomain in the posterior neighborhood did not result in mislocalization of AIB (Supplementary Fig. 8A,B).

AIB neurite placement by retrograde zippering, and presynaptic assembly are coordinated during development

AIB displays a polarized distribution of pre- and postsynaptic specializations, and these specializations specifically localize to the neurite segments occupying the anterior and posterior neighborhoods, respectively. The placement of the AIB neurite in the anterior and posterior neighborhoods and its synaptic polarity underlies its role as a connector hub across layers (Sabrin et al., 2019, Towlson et al., 2013). To understand how the distribution of presynaptic specializations relates to the placement of the AIB neurite, we imaged the subcellular localization of presynaptic protein RAB-3 during AIB embryonic development. We observed that presynaptic proteins populate the AIB neurite starting from the tip towards the dorsal midline, in a retrograde pattern reminiscent of the retrograde zippering that places the AIB neurite in the anterior neighborhood (Fig. 7A-I). The timing of formation of presynaptic sites suggested that that the process of synaptogenesis closely followed the retrograde zippering mechanisms of AIB repositioning, indicating that zippering, and presynaptic assembly, coincide during development. Consistent with the importance of AIB neurite placement in the anterior neighborhood for correct synaptogenesis, we observed that in *syg-1(ky652)*, RAB-3 signal was specifically and consistently reduced in regions of the AIB distal neurite incapable of repositioning to the anterior neighborhood (Supplementary Fig. 8C-N). Overall, our study identified a role for differential adhesion in regulating neurite placement via retrograde zippering, which in turn influences synaptic specificity onto target neurons (Fig. 7J).

Discussion

The precise assembly of the cellular architecture of AIB in the context of the layered nerve ring neuropil underwrites its role as a "rich-club" neuron. AIB was identified, through graph theory analyses, as a rich-club neuron (Towlson et al., 2013) - a connector hub with high betweeness centrality, which links nodes of the *C. elegans* neural networks with high efficiency. We observe that the AIB neurite segments are precisely placed on distinct functional layers of the nerve ring neuropil, and that the placement of these segments, in the context of the pre- and postsynaptic polarity of the neurite, enables AIB to receive inputs from one neighborhood and relay information to the other, thereby linking otherwise modular and functionally distinct layers. Our connectomic analyses and *in vivo* imaging reveal that these features of AIB architecture are stereotyped across examined *C. elegans* animals, even as early as the first larval stage, L1. They are also evolutionarily conserved in nematodes, as examination of AIB in the connectome of the nematode *Pristionchus pacificus,* which is separated from *C. elegans* by 100 million years of evolutionary time, revealed similar design principles (Hong et al., 2019). The architecture of AIB is reminiscent to that seen for other "nexus neurons" in layered neuropils, such as AII amacrine cells in the inner plexiform layer of the vertebrate retina (Marc et al., 2014). Like AIB, All amacrine cells receive inputs from one laminar neighborhood (rod bipolar axon terminals in "lower sublamina b") and produce outputs onto a different neighborhood (ganglion cell dendrites in "sublamina a") (Kolb, 1995, Strettoi et al., 1992). For these nexus neurons, as for AIB, the precise placement within neuropil layers is critical for their function and connectivity. We now demonstrate that for AIB, this precise placement is governed via differential adhesion instructed by the layer-specific expression of IgCAM SYG-1. Interestingly, other 'rich-

443 club' neurons that emerged from connectomic studies, such as AVE and RIB, are also
444 placed along SYG-1-expressing nerve ring layers, suggesting that similar, SYG-1
445 dependent and layer-specific mechanisms could underpin placement of these neurons.

446 Differential adhesion acts via retrograde zippering mechanisms to position AIB
447 across multiple and specific layers. We established new imaging paradigms to
448 document *in vivo* embryonic development of AIB, and observed that the sorting of its
449 distal neurite segment onto the anterior neighborhood occurs, not via tip-directed
450 fasciculation as we had anticipated, but via neurite-shaft retrograde zippering. Zippering
451 mechanisms had been previously documented (Barry et al., 2010, Voyiadjis et al.,
452 2011), and modeled, for tissue culture cells, where they were shown to act via
453 biophysical forces of tension and adhesion (Smit et al., 2017). We now demonstrate that
454 retrograde zippering also acts *in vivo* to precisely place segments of the AIB neurite in
455 specific neuropil layers.

456 Retrograde zippering depends on differential adhesion across layers, and is
457 instructed by the dynamic expression of SYG-1, and its interaction with the SYG-2
458 expressing AIB neurons. The observed role of SYG-1 in the nerve ring is reminiscent of
459 the role of the SYG-1 and SYG-2 mammalian orthologs, Kirrel2 and Kirrel3, in axon
460 sorting in the olfactory system (Serizawa et al., 2006), and consistent with observations
461 in *C. elegans* that *syg-2* loss of function mutants result in defasciculation defects of the
462 HSNL axon (Shen et al., 2004). Our findings are also consistent with studies on the
463 roles of SYG-1 and SYG-2 Drosophila orthologues, Hibris and Roughest, in tissue
464 morphogenesis of the pupal eye (Bao and Cagan, 2005). In these studies, Hibris and
465 Roughest were shown to instruct complex morphogenic patterns by following simple,

466 adhesion and surface energy-based biophysical principles that contributed to
467 preferential adhesion of specific cell types. We now demonstrate that similar biophysical
468 principles of differential adhesion might help organize neurite placement within
469 heterogeneous tissues, such as neuropils in nervous systems.

470 SYG-1 and SYG-2 coordinate developmental processes that result in synaptic
471 specificity for the AIB interneurons. Synapses in *C. elegans* are formed *en passant*, or
472 along the length of the axon, similar to how they are assembled in the CNS for many
473 circuits (Jontes et al., 2000, Koestinger et al., 2017). Placement of neurites within
474 layers therefore restrict synaptic partner choice. We examined how these events of
475 placement, and synaptogenesis, were coordinated for the AIB interneurons and
476 observed coincidence of presynaptic assembly and retrograde zippering of the AIB
477 neurite. SYG-1 and SYG-2 were identified in *C. elegans* for their role in synaptic
478 specificity (Shen and Bargmann, 2003, Shen et al., 2004), and the assembly of synaptic
479 specializations can result in changes in the cytoskeletal structure and adhesion
480 junctions (Missler et al., 2012). We hypothesize that coordinated assembly of synaptic
481 sites during the process of retrograde zippering could provide forces that stabilize
482 zippered stretches of the neurite. These could in turn “button” and fasten the AIB neurite
483 onto the anterior layer, securing its relationship with its postsynaptic partner. Consistent
484 with this hypothesis, we observe that ablation of one of its main postsynaptic partners,
485 the RIM neurons, results in defects in AIB placement in the anterior neighborhood.
486 Given the important role of adhesion molecules in coordinating cell-cell interactions and
487 synaptogenesis (Sanes and Zipursky, 2010, Sanes and Zipursky, 2020, Tan et al.,
488 2015, Yamagata and Sanes, 2008, Yamagata and Sanes, 2012), we speculate that

adhesion molecules involved in synaptogenesis and neurite placement within layered neuropils might similarly act to coordinate differential adhesion and synaptogenesis onto target neurons.

Zippering mechanisms via affinity-mediated adhesion might help instruct neighborhood coherence while preserving 'fluid', or transient interactions among neurites within neuropil structures. Analysis of connectome data and examination of neuronal adjacencies within the nerve ring neuropil revealed that contact profiles for single neurons vary across animals indicative of fluid or transient interactions during development (Moyle et al., 2021). Yet neuropils have a stereotyped and layered architecture encompassing specific circuits. We hypothesize that dynamic expression of adhesion molecules help preserve tissue organization in tangled neuropils via the creation of affinity relationships of relative strengths. These relationships, in the context of outgrowth decisions of single neurites, would contribute to the sorting of neurites onto specific strata. We propose that sorting of neurite into strata would happen through biophysical interactions not unlike those reported for morphogenic events in early embryos and occurring via differential adhesion (Steinberg, 1962, Foty and Steinberg, Steinberg and Gilbert, 2004). Spatiotemporally restricted expression of CAMs in layers, as we observe for SYG-1 and has been observed for other CAMs in layered neuropils (Sanes and Zipursky, 2010, Sanes and Zipursky, 2020, Tan et al., 2015, Yamagata and Sanes, 2008, Yamagata and Sanes, 2012) would then result in dynamic affinity-mediated relationships that preserve neighborhood coherence in the context of 'fluid', or transient interactions among neurites within the neuropil structures.

Methods

Materials Availability

Plasmids and worm lines generated in this study are available upon request (see Supplementary Tables 2 and 3 for details).

Data Availability

The original/source data generated or analyzed during this study are available from the corresponding author upon request.

Code Availability

From previously determined adjacencies (Brittin et al., 2018, Brittin et al., 2021, Witvliet et al., 2020), cosine similarities were calculated in Excel, using the formula described in Methods. For computing binary connection matrices for centrality analysis (detailed in Methods below). we used the function “betweenness_bin.m” in the Brain Connectivity Toolbox (Rubinov and Sporns) of MATLAB2020.

Maintenance of *C. elegans* strains

C. elegans strains were raised at 20°C using OP50 *Escherichia coli* seeded on NGM plates. N2 Bristol is the wild-type reference strain used. Plasmids and transgenic strains generated and used in this study (Supplementary Tables 2 and 3) are available upon request.

Molecular biology and generation of transgenic lines

We used Gibson Assembly (New England Biolabs) or the Gateway system (Invitrogen) to make plasmids (Supplementary Table 3) used for generating transgenic *C. elegans* strains (Supplementary Table 2). Detailed cloning information or plasmid maps will be provided upon request. Transgenic strains were generated via microinjection with the construct of interest at 2-100 ng/uL by standard techniques (Mello and Fire). Co-injection markers *unc-122p*: GFP or *unc-122p*: RFP were used.

We generated the *syg-1* transcriptional reporter (Fig. 5, Supplementary Fig. 5) by fusing membrane-targeted PH:GFP to a 3.5 kb *syg-1* promoter region as described (Schwarz et al., 2009). The translational reporter was generated by fusing a GFP-tagged *syg-1b* cDNA using the same promoter (Fig. 5). For cell-specific SYG-1 expression, full length SYG-1, SYG-1 ecto (extracellular +TM domain - amino acids 1-574, (Chao and Shen, 2008)) or SYG-1 endo (signal peptide+TM domain+cytoplasmic domain – amino acids 1-31+526-574) were used.

For cell-specific labeling and expression in larvae, we used an *inx-1* promoter for AIB (Altun et al., 2008), a *ceh-36* promoter for AWC and ASE (Kim et al., 2010) and *tdc-1*, *gcy-13* and *cex-1* promoters for RIM (Greer et al., 2008, Piggott et al., 2011).

SNP mapping and Whole-Genome Sequencing

We performed a visual forward genetic screen in an integrated wild type transgenic strain (*olaIs67*) with AIB labeled with cytoplasmic mCherry and AIB presynaptic sites labeled with GFP:RAB-3. Ethyl methanesulfonate (EMS) mutagenesis was performed and animals were screened for defects in placement of the AIB neurite,

556 or presynaptic distribution. We screened for these same phenotypes in our reverse
557 genetic screens as well, where we crossed the marker strain (*olaIs67*) to characterized
558 mutant alleles. We screened F2 progeny on a Leica DM 5000 B compound microscope
559 with an HCX PL APO 63x/1.40–0.60 oil objective.

560 Mutants from forward genetic screens were out-crossed six times to wild type
561 (N2) animals and mapped via single-nucleotide polymorphism (SNP) (Davis et al.,
562 2005) and whole-genome sequencing as previously described (Sarin et al., 2008). We
563 analyzed the results using the Galaxy platform (https://galaxyproject.org/news/cloud-
564 map/, EMS variant density mapping workflow (Minevich et al., 2012).

565

566 **Confocal imaging of *C. elegans* larvae and image processing**

567 We used an UltraView VoX spinning disc confocal microscope with a 60x CFI
568 Plan Apo VC, NA 1.4, oil objective on a NikonTi-E stand (PerkinElmer) with a
569 Hamamatsu C9100–50 camera. We imaged the following fluorescently tagged fusion
570 proteins, eGFP, GFP, PH:GFP (membrane-tethered), RFP, mTagBFP1, mCherry,
571 mCherry:PH, mScarlet, mScarlet:PH at 405, 488 or 561 nm excitation wavelength. We
572 anesthetized larval stage 4 animals (unless otherwise mentioned) at room temperature
573 in 10mM levamisole (Sigma) and mounted them on glass slides for imaging. For Fig. 5
574 and the RIM neuron ablation images in Supplementary Fig. 7, larval stage 3 animals
575 were imaged.

576 We used the Volocity image acquisition software (Improvision by Perkin Elmer)
577 and processed our images using Fiji (Schindelin et al., 2012). Image processing

included maximum intensity projection, 3D projection, rotation, cropping, brightness/contrast, line segment straightening, and pseudo coloring. All quantifications from confocal images were conducted on maximal projections of the raw data. Pseudocoloring of AIBL and AIBR was performed in Fiji. To achieve this, pixels corresponding to the neurite of either AIBL/R were identified and the rest of the pixels in the image were cleared. This was done for both neurons of the pair and the resulting images were merged. For quantifications from confocal images, n= number of neurons quantified, unless otherwise mentioned.

Embryo labeling, imaging and image processing

For labeling of neurites in embryos, we used membrane tethered PH:GFP or mScarlet:PH. A subtractive labeling strategy was employed for AIB embryo labeling (Supplementary Fig. 3A-C) (Armenti et al., 2014, Moyle et al., 2021). Briefly, we generated a strain containing unc-42p::ZF1::PH::GFP and lim-4p::SL2::ZIF-1, which degraded GFP in the sublateral neurons, leaving GFP expression only in the AIB and/or ASH neurons. Onset of twitching was used as a reference to time developmental events. Embryonic twitching is stereotyped and starts at 430 minutes post fertilization (m.p.f) for our imaging conditions.

Embryonic imaging was performed via dual-view inverted light sheet microscopy (diSPIM) (Kumar et al., 2014, Wu et al., 2013) and a combined triple-view line scanning confocal/DL for denoising (Wu et al., in prep, also described below) described below. Images were processed and quantifications from images were done using CytoSHOW,

an open source image analysis software. CytoSHOW can be downloaded from http://www.cytoshow.org/ as described (Duncan et al., 2019).

Triple-view line-scanning confocal/DL

We developed a triple-view microscope that can sequentially capture three specimen views, each acquired using line-scanning confocal microscopy (Wu et al., in prep). Multiview registration and deconvolution can be used to fuse the 3 views (Wu et al., 2016), improving spatial resolution. Much of the hardware for this system is similar to the previously published triple-view system (Wu et al., 2016), i.e., we used two 0.8 NA water immersion objectives for the top views and a 1.2 NA water immersion lens placed beneath the coverslip for the bottom view. To increase acquisition speed and reduce photobleaching, we applied a deep-learning framework (Weigert et al., 2018) to predict the triple-view result when only using data acquired from the bottom view. The training datasets were established from 50 embryos (anesthetized with 0.3% sodium azide) in the post-twitching stage, in which the ground truth data were the deconvolved triple view confocal images, and the input data were the raw single view confocal images. These approaches resulted in improved resolution (270nm X 250 nm X 335nm).

Cell lineaging

Cell lineaging was performed using StarryNite/AceTree (Bao et al., 2006, Boyle et al., 2006, Murray et al., 2006). Light sheet microscopy and lineaging approaches were integrated to uncover cell identities in pre-twitching embryos (Duncan et al., 2019).

Lineaging information for promoters is available at http://promoters.wormguides.org. Our integrated imaging and lineaging approaches enabled us to identify a promoter region of *inx-19* which is expressed in the RIM neurons prior to RIM neurite outgrowth (~370 m.p.f.) and in additional neurons in later embryonic stages. The *inx-19p* was one of the promoters used for embryonic ablation of the RIM neurons (described in the next section).

In addition, our integrated imaging and lineaging approach also enabled us to identify two promoters with expression primarily in neurons located at the AIB posterior neighborhood (*nphp-4*p and *mgl-1b*p). 4/4 neuron classes that were identified to have *nphp4*p expression are in the AIB posterior neighborhood (ADL/R, ASGL/R, ASHL/R, ASJL/R) and 2/3 neuron classes that were identified to have *mgl-1b*p expression are in the AIB posterior neighborhood (AIAL/R, ADFR) (http://promoters.wormguides.org). We used these promoters to drive ectopic expression of a *syg-1* cDNA specifically in the posterior neighborhood.

Caspase-mediated ablation of RIM neurons

The RIM neurons were ablated using a split-caspase ablation system (Chelur and Chalfie, 2007). We generated one set of transgenic strains with co-expression of the p12 and p17 subunit of human Caspase-3, both expressed under *inx-19p* (termed ablation strategy 1), and another set of ablation strains with co-expression of the p12 subunit expressed under *inx-19p* and p17 under *tdc-1p* (termed ablation strategy 2) (Supplementary Fig. 7). L3 larvae from the RIM-ablated populations were imaged on the

spinning-disk confocal microscope (described in the **'Confocal imaging of C. elegans larvae and image processing'** section).

Rendering of neurites and contacts in the EM datasets

From available EM datasets (Brittin et al., 2018, Cook et al., 2019, White et al., 1986, Witvliet et al., 2020) we rendered the segmentations of neuron boundaries in 2D using TrakEM2 in Fiji. TrakEM2 segmentations were volumetrically rendered by using the 3D viewer plugin in Fiji (downloaded from https://imagej.net/Fiji#Downloads) and saved as object files (.obj), or by using the 3D viewer in CytoSHOW.

To generate 3D mappings of inter-neurite membrane contact, the entire collection of 76,046 segmented neuron membrane boundaries from the JSH TEM datasets (Brittin et al., 2018, White et al., 1986) were imported from TrakEM2 format into CytoSHOW as 2D cell-name-labelled and uniquely color-coded regions of interest (ROIs). To test for membrane juxtaposition, we dilated each individual cell-specific ROI by 9 pixels (40.5 nm) and identified for overlap by comparing with neighboring undilated ROIs from the same EM slice. A collection of 289,012 regions of overlap were recorded as new ROIs, each bearing the color code of the dilated ROI and labeled with both cell-names from the pair of the overlapped ROIs. These "contact patch" ROIs were then grouped by cell-pair-name and rendered via a marching cubes algorithm to yield 3D isosurfaces saved in .obj files. Each of the 8852 rendered .obj files represents all patches of close adjacency between a given pair of neurons, color-coded and labeled by cell-pair name. Selected .obj files were co-displayed in a CytoSHOW3D viewer window to produce views presented in Fig. 1, Supplementary Fig. 1 and 2.

668

669 **Schematic representation of larval *C. elegans***

670 The schematic representations of larval *C. elegans* in Fig. 1 and Supplementary Fig. 6
671 were made using the 3D worm model in OpenWorm (http://openworm.org - 3D Model
672 by Christian Grove, WormBase, CalTech).

673

674 **Quantification and statistical analysis**

675

676 **Cosine similarity analysis for comparing AIB contacts across connectomes**

677 We performed cosine similarity analysis (Han et al., 2012) on AIB contacts in
678 available connectome datasets (Brittin et al., 2018, White et al., 1986, Witvliet et al.,
679 2020). For each available adjacency dataset (Brittin et al., 2021, Moyle et al., 2021,
680 Witvliet et al., 2020), we extracted vectors comprising of the weights of AIB contacts
681 with neurons common to all the datasets. We then performed cosine similarity analysis
682 on these vectors using the formula:

683 $$\frac{\sum_{i=1}^{n} A_i B_i}{\sqrt{\sum_{i=1}^{n} A_i^2}\sqrt{\sum_{i=1}^{n} B_i^2}}$$

684 where A and B are the two vectors under consideration with the symbol “i” denoting the
685 i-th entry of each vector. The similarity values were plotted as a heat map for AIBL and
686 AIBR using Prism. For the datasets L1_0hr, L1_5hr, L1_8hr, L2_23hr, L3_27hr, L4_JSH
687 and Adult_N2U, only the neuron-neuron contacts in the EM sections corresponding to
688 the nerve ring were used (as opposed to the whole connectome).

Betweenness centrality analysis

We analyzed betweenness centrality for two of the available connectomes of different developmental stages (L1 and adult) (Witvliet et al., 2020). By treating individual components (mostly neurons) of a connectome as the vertices of a graph, we use the following definition of Betweenness Centrality for a vertex v,

$$BC(v) = \sum_{s,t:s\neq t\neq v} \frac{\lambda_{st}(v)}{\lambda_{st}}$$

Here $\lambda_{st}(v)$ denotes the number of shortest paths between the vertices s and t, that include vertex v, whereas λ_{st} denotes the total number of shortest paths between the vertices s and t. We finally divide $BC(v)$ by $(N-1)(N-2)/2$ to normalize it to lie between 0 and 1. For our implementation we use the Brain Connectivity Toolbox (Rubinov and Sporns) of MATLAB2020, in particular, the function “betweenness_bin.m” in which we input the binary connectivity matrix (threshold = 0) (Fornito et al., 2016) corresponding to the L1 and adult connectomes (Witvliet et al., 2020). We made a Prism box plot (10 to 90 percentile) of betweenness centrality values of all components in each of the two connectomes and highlighted the betweenness centrality values for AIBL and AIBR.

Representation of AIB from confocal images

Since we observed that the proximal and distal neurites of AIBL and AIBR completely align and overlap (Supplementary Fig. 1) in confocal image stacks where the worms are oriented on their side, for representation purposes we have used the upper 50% of z-slices in confocal image stacks to make maximum intensity projections. This shows the proximal neurite of AIBL in the context of the distal of AIBR (which has the same anterior-posterior position as the distal neurite of AIBL) (Supplementary Fig. 1), or vice versa.

Quantification of penetrance of AIB neurite placement defects and gain-of-function phenotypes

The penetrance of defects in AIB neurite placement in the anterior neighborhood in mutant (or ablation) strains was determined by visualizing the AIB neurite and scoring animals with normal or defective anterior neighborhood placement under the Leica compound microscope described. Animals in which the entire distal neurite was placed at a uniform distance from the proximal neurite, for both AIBL and AIBR, were scored as having normal AIB distal neurite placement.

The penetrance of the gain-of-function effects in ectopic SYG-1 expression strains was determined by scoring the percentage of animals showing ectopic AIB distal neurite placement in the posterior neighborhood. Animals with part (or whole) of the AIB distal neurite overlapping with the posterior neighborhood were considered as having ectopic AIB placement.

Quantification of minimum perpendicular distance between neurites

Minimum perpendicular distances between neurites were measured by creating a straight line selection (on Fiji) between the neurites (perpendicular to one of the neurites) in the region where the gap between them is estimated to be the smallest. The measurements were done on maximum intensity projections of raw confocal image stacks where the worms are oriented on their side (z-stacks acquired along left-right axis of the worm, producing a lateral view of the neurons).

Quantification of percent detachment between neurites

The percent detachment for defasciculated neurites (AIB and RIM) is calculated by the formula % detachment = detached length (L_d) x 100 /total length (L_t) (also shown in Fig. 4M). L_d is calculated by making a freehand line selection along the detached region of the RIM neurite and measuring its length and L_t is calculated by making a freehand selection along the RIM neurite for the entire length over which it contacts AIB, and measuring the length of the selection. All the measurements were performed on maximum intensity projections of confocal image stacks where the worms are oriented on their side (z-stacks acquired along left right axis of the worm, producing a lateral view of the neurons).

Quantification of relative enrichment of *syg-1* reporter expression in the anterior neighborhood

Relative (anterior) enrichment of *syg-1* reporter expression in embryos (Fig. 5S) is calculated using the formula, relative enrichment (*syg-1p*) = mean anterior neighborhood intensity (I_a)/mean posterior neighborhood intensity (I_p). These measurements were done in transgenic embryos co-expressing the AIB reporter and the *syg-1* transcriptional reporter. For calculation of I_p, a freehand line selection was made (using CytoSHOW, http://www.cytoshow.org/, (Duncan et al., 2019)) along the posterior band of *syg-1* expression and mean intensity along the selection was calculated. Same was done for calculation of I_a. The ratios of I_a and I_p were plotted as relative (anterior) enrichment values (Fig. 5S). These values were calculated from 3D projections of deconvolved diSPIM images acquired at intensities within dynamic range (not saturated) at timepoints during embryogenesis (485, 515 and 535 minutes post fertilization), when the AIB neurite grows and is placed into the posterior and anterior neighborhoods. I_a/I_p was calculated from the anterior and posterior *syg-1* bands on each side of the embryonic nerve ring per embryo (number of embryos = 4, number of I_a/I_p values = 8).

Quantification of the dorsal midline shift (chiasm) length of AIB

The dorsal midline shift (chiasm) lengths of AIB and AVE were calculated by making 3D maximum intensity projections of confocal z-stacks and orienting the neuron pair to a dorsal-ventral view. A straight line selection is made along the posterior-anterior shift of each neuron, and each arm of the “X” of the chiasm was measured (using Fiji).

Quantification of distal neurite length of AIB

The length of the distal neurite of AIB was measured by drawing a freehand line along the neurite segment occupying the distal neighborhood (including the chiasm) in maximum intensity projections of confocal image stacks where the worms are oriented on their side (z-stacks acquired along left-right axis of the worm, producing a lateral view of the neurons).

Quantification of positions and velocities of the AIB neurite during embryogenesis

The positions of the AIB neurite in the anterior and posterior neighborhoods in Fig. 3C are calculated from deconvolved maximum intensity projections of diSPIM images where the neurons are oriented in an axial view. These positions are determined by measuring the lengths along the AIB neurite from the unzippering/zippering forks to the dorsal midline. The distance of the zippering fork from the midline is subtracted from the total length of the neurite at the start of zippering, to obtain the length of the AIB neurite that has already zippered. The fraction of the length of the AIB neurite that has zippered to the initial length of the relocating AIB distal neurite, multiplied by 100, yields the percentage of the AIB neurite that has zippered at each timepoint. The reported values (in Fig. 5S) of the percentages of the AIB neurite that has zippered are averages across the three independent embryo datasets (used for the Fig. 3 plots). Embryos in which the AIB and RIM neurons were specifically labeled by the subtractive labeling strategy were

used for the analysis. Reported measurements represent AIB neurites which were visible through the imaging window. Zippering velocity (Fig. 3D) at any timepoint (t1) is defined as the difference between positions of the AIB neurite at that timepoint (t1) and the next timepoint (t2) (for which position was measured), divided by the time interval (t2-t1). These measurements are performed with CytoSHOW. To pseudocolor the neurites for representation, we used the same steps described in **'Confocal imaging of *C. elegans* larvae and image processing.'**

Quantification of the angle of exit of the developing AIB distal neurite with the ventral turn of the nerve ring in the posterior neighborhood

The angle of exit (α) of the developing AIB distal neurite is measured as the angle between straight line tangents drawn along the separating distal segment of AIBL and the proximal neurite of AIBR and vice versa. These measurements are performed on deconvolved maximum intensity projections of diSPIM images where the neurons are oriented in an axial view. The angle of ventral turn of the nerve ring (β) is measured as the angle between straight line tangents drawn along segments of the nerve ring on either side of the ventral bend of the nerve ring in the posterior neighborhood (see Supplementary Fig. 3G,H). β is measured from images of embryos with proximal neighborhood labeled with *nphp-4* promoter (see Results and http://promoters.wormguides.org). All measurements are performed using CytoSHOW.

Imaging and representation of synaptic protein RAB-3 in AIB in embryos

817 Time-lapse imaging of presynaptic protein RAB-3 in AIB in embryos was
818 performed using diSPIM (Wu et al., 2013). To visualize the distribution of RAB-3 along
819 the neurite we straightened the distal neurite of each AIB neuron from maximum
820 intensity projections where the AIB neurons are oriented in the axial view (Fig. 7).

821

822 **Quantification of nerve ring width from larval stage animals**

823 The nerve ring was visualized using a 5.6 kb promoter of *cnd-1* (Shah et al., 2017)
824 driving membrane-targeted GFP (PH:GFP) in wildtype and *syg-1(ky652)* mutant
825 animals. Measurements were done on confocal image stacks where the worms are
826 oriented on their side (z-stacks acquired along left-right axis of the worm, producing a
827 lateral view of the neurons). On each side of the worm a straight line selection along the
828 anterior-posterior axis from one edge of the labeled nerve ring to the other was defined
829 as the nerve ring width.

830

831 **Quantification of length of the dorsal midline shift (chiasm) from EM images**

832 From a segmented EM dataset of the L4 larva JSH (Brittin et al., 2018, White et
833 al., 1986), we calculated the number of z-slices containing segmented regions of the
834 anterior-posterior shift (that forms the chiasm) of AIBL. We multiplied this number with
835 the z-spacing of the dataset (60 nm) to obtain the anterior-posterior distance that the
836 AIBL shift spans (d_z). We then calculated the x-y distance between the segmented
837 regions of the AIBL shift in the topmost and bottommost z-slice($d_{x\text{-}y}$). We calculate the
838 length of the shift in 3D (l) using the formula

$$\boldsymbol{l} = \sqrt{d_z^2 + d_{x-y}^2}$$

The same measurements were repeated for the length of the dorsal midline shift of AIBR.

Statistical analyses

Statistical analyses were conducted with PRISM 7 software. For each case, the chosen statistical test is described in the figure legend and "n" values are reported. Briefly, for continuous data, comparisons between two groups were determined by unpaired two-tailed t-test and comparisons within multiple groups were performed by ordinary one-way ANOVA. Error bars were reported as standard error of the mean (SEM). For categorical data, groups were compared with two-sided Fisher's exact test. The range of p-values for significant differences are reported in the figure legend. The Cohen's d statistic was determined for comparisons between continuous datasets with statistically significant differences, to obtain estimates of effect sizes.

Acknowledgements

We thank Kang Shen, Harald Hutter and John Murray for providing strains and constructs. We thank Scott Emmons, Steve Cook, and Chris Brittin, and Mei Zhen and Daniel Witvliet for sharing their segmented EM data and adjacencies. We thank Thierry Emonet and members of the Colón-Ramos lab for help, advice and insightful comments during manuscript preparation. We thank Sarah Se-Hyun Jho and Kenya Collins for their

contributions to the project. We thank the Caenorhabditis Genetics Center (funded by NIH Office of Research Infrastructure Programs P40 OD010440) for *C. elegans* strains. We thank the Research Center for Minority Institutions program, the Marine Biological Laboratories (MBL), and the Instituto de Neurobiología de la Universidad de Puerto Rico for providing meeting and brainstorming platforms. H.S. and D.A.C-R. acknowledge the Whitman and Fellows program at MBL for providing funding and space for discussions valuable to this work. Research in the D.A.C-R., W.A.M., and Z. B. labs were supported by NIH grant No. R24-OD016474. M.W.M. was supported by NIH by F32-NS098616. Research in H.S. lab was further supported by the intramural research program of the National Institute of Biomedical Imaging and Bioengineering (NIBIB), NIH. Research in Z.B. lab was further supported by an NIH center grant to MSKCC (P30CA008748). Research in the D.A.C.-R. lab was further supported by NIH R01NS076558, DP1NS111778 and by an HHMI Scholar Award.

Author contributions

T.S. and D.A.C.-R. designed the experiments. T.S. performed the experiments and data analysis. X.H., Y.W. and H.S. designed and performed the triple-view confocal imaging and deep learning analysis. T.S., N.L.K., M.W.M., L.H.D., and N.V.-M. generated reagents and provided resources. T.S., N.L.K., M.W.M., L.S., Y.W., A.S., Z.B., H.S. and W.A.M developed, and designed methodologies used in the study. S.E.E. analyzed and interpreted embryonic transcriptomics data (Packer et al., 2019). L.F. and A.S. contributed lineaging data and expertise. T.S. and D.A.C.-R. prepared the manuscript with input from the other authors. Z.B., W.A.M., H.S., D.A.C.-R. supervised the project.

Declaration of interests

The authors declare no competing interests.

Figure Legends

Fig. 1: AIB single neurite is placed along two distinct neighborhoods in the nerve ring

A, Schematic of an adult/larval *C. elegans* showing an AIB neuron (cyan) and its posterior (orange) and anterior (magenta) neighborhoods in the head. The AIB neurite has a proximal neurite segment (orange arrow), a posterior-anterior shift at the dorsal midline (dashed line) and a distal neurite segment (magenta arrow; on the other side of the worm, behind the pharynx, which is in gray). The neon-colored outline represents the nerve ring neuropil. The terms 'proximal' or 'distal' neurite segments refer to the relationship of the neurite segment to the AIB cell body. The neighborhoods in which the 'proximal' and 'distal' neurite segments are positioned are referred to as the 'posterior' or 'anterior' neighborhoods, respectively, because of their position along the anterior-posterior axis of the worm. Note that this schematic only shows one neuron of the AIB pair. Cell body is marked with an asterisk.

B, Magnified schematic of AIB and its neighborhoods in **A**

C, Representative confocal image showing the lateral view of an AIB neuron labeled with cytoplasmic mCherry (cyan).

D, Representative confocal image showing an AIB neuron labeled with cytoplasmic mCherry (cyan); and RIM motor neuron of the anterior neighborhood labeled with cytoplasmic GFP (magenta) in lateral view. Note the colocalization of the AIB distal neurite (but not the proximal neurite) with the anterior neighborhood marker RIM (compare with **E**).

E, As **D**, but with AIB (cyan) and AWC and ASE sensory neurons of the posterior neighborhood (orange). Note the colocalization of the AIB proximal neurite (but not the distal neurite) with the posterior neighborhood markers AWC and ASE (compare with **D**).

F-J, Same as **A-E** but in axial view indicated by the arrow in **F**. Note shift in **H** (arrows), corresponding to AIB neurite shifting neighborhoods (compare **I** and **J**).

K,L, Volumetric reconstruction from the JSH electron microscopy connectome dataset (White et al., 1986) of AIBL (**K**), and AIBL overlaid on nerve ring strata **(L)**, in lateral view, with S2 and S3 strata (named as in (Moyle et al., 2021)), containing anterior and posterior neighborhoods, respectively.

M, Volumetric reconstruction of AIBL and AIBR in axial view (from the JSH dataset (White et al., 1986)). Note the shift in neighborhoods by AIBL and AIBR, at the dorsal midline (dashed line), forms a chiasm.

N, Schematic of **M,** highlighting the AIB neighborhoods for context and the dorsal midline with a dashed line.

Scale bar = 10 μm for **A-J** and 3 μm for **K-N**.

Fig. 2: A retrograde zippering mechanism positions the AIB neurites in the anterior neighborhood during embryonic development

A, Schematic of axial view of the AIB neuron pair: AIBL (cyan) and AIBR (yellow) in the context of the nerve ring (light neon) and the pharynx (grey), with posterior neighborhood labeled (orange) and the dashed line representing the dorsal midline where the AIB chiasm is present in adults (see Fig. 1). Dotted box represents region in **B'-F'**, and dotted box in **G.**

B,F, Time-lapse showing initial placement of AIBL and AIBR in the posterior neighborhood and their subsequent separation from this neighborhood. Images are deconvolved diSPIM maximum intensity projections obtained from developing embryos. Neurons were individually pseudocolored to distinguish them (see Methods). The dorsal half of the nerve ring (dotted box in **A**) are magnified in **B'-F'**. **B''-F''** are schematic diagrams representing the images in **B-F**. Dashed vertical lines represent the dorsal midline. Note in (**B, B', B''**), the AIBL and AIBR neurites approaching the dorsal midline in the posterior neighborhood. In (**C, C', C''**), AIBL and AIBR have met at the dorsal midline and continue growing along each other, past the midline. The latter part of the neurite, past the midline, becomes the future distal neurite. (**D, D', D''**) shows the tip of the AIBL future distal neurite moving away from the posterior neighborhood and its counterpart, AIBR. The arrowhead indicates the point of separation of the AIBL distal neurite and the AIBR proximal neurite. (**E, E', E''**) shows further separation of the two neurites and by (**F, F', F"**), they have completely separated. The arrowheads in (**E, E', E''**) and (**F, F', F''**) also indicate the junction between the separating AIBL distal neurite

and the AIBR proximal neurite. A similar sequence of events is visualized at higher spatial resolution in Supplementary Fig. 3 using triple-view line scanning confocal microscopy.

G, G', Confocal micrograph of a postembryonic L4 animal (axial view) showing the relationship between AIBL and AIBR. The region in the box represents the dorsal part of the nerve ring, magnified in **G'**.

H, Axial view schematic of one AIB neuron (cyan) in the context of the anterior neighborhood marker, the RIM neuron (magenta), the nerve ring (light neon) and the pharynx (grey).

I-K, Time-lapse showing placement of the AIB neurite (cyan) relative to the anterior neighborhood (magenta). As in **B-F**, images are deconvolved diSPIM maximum intensity projections and the neurons were pseudocolored. The dorsal half of the nerve ring (dotted box in **H**) are magnified in **I'-K'**. Dashed line indicates dorsal midline (where the shift, or chiasm, in the adult is positioned, see Fig. 1). **I''-K''** are schematic diagrams representing the images in **I-K**.

Note in (**I, I', I"**), the tip of the AIB neurite encounters the RIM neurite in the anterior neighborhood (green arrowhead). In (**J, J', J''**), the AIB distal neurite has partially aligned along the RIM neurites. The green arrowhead now indicates point of initial encounter of the two neurites (same as in **I**'), and the red arrowhead indicates the retrograde zippering event bringing the AIB and RIM neurons together in the anterior neighborhood. In (**K, K', K"**) the two neurites have zippered up to the dorsal midline. Arrow in **J'** indicates direction of zippering.

L, Confocal micrograph of a postembryonic L4 animal in axial view showing the final position of AIB with respect to the anterior neighborhood. The same image as Fig. 1I was used here for reference. The region in the dotted box represents dorsal part of the nerve ring, magnified in (**L'**).

M, Schematic highlights the steps by which the AIB distal neurite is repositioned to a new neighborhood – (i) exit from the posterior neighborhood and (ii) retrograde zippering onto the anterior neighborhood with intermediate partially zippered states and completely zippered states.

Scale bar = 10 μm for **B-G** and **I-L**.

Scale bar = 2 μm for **B'-G'** and **I'-L'**

Times are in m.p.f. (minutes post fertilization).

Fig. 3: Biophysical modeling of AIB developmental dynamics is consistent with differential adhesion leading to retrograde zippering

A, Axial view schematic of a single AIB neuron during transition of its neurite between the posterior (orange) and anterior (magenta) neighborhoods.

B,B' Magnified schematic of dotted inset in (**A**) showing the AIB neurite (cyan) during its transition from the posterior to the anterior neighborhood. The lengths of the neurite positioned in the posterior and anterior neighborhoods are denoted by L_p and L_a, respectively. The velocity with which the AIB neurite zippers onto the anterior neighborhood is denoted by v_{zip}, and the velocity with which it unzippers from the posterior neighborhood is denoted by v_{unzip}. At the junction between the neurite and the

two neighborhoods, i.e., at the zippering and unzippering forks, tension and adhesion forces act on the neurite (see **B'** and Supplementary Note 1). **B',** Schematic of AIB neurite zippering to the anterior neighborhood. Adhesion $S_{anterior}$ acts in the direction of zippering (and therefore in the direction of the zippering velocity v_{zip}), and favors zippering. Tension $T_{anterior}$ acts in the opposite direction, disfavoring zippering.

C, Plot of position vs. time of the AIB neurite in both neighborhoods in synchronized embryos at the indicated timepoints on the x-axis (±5 mins). Plot shows mean of L_p (n=4) and L_a (n=3) values at different timepoints. Note zippering from the anterior neighborhood and unzippering from the posterior neighborhood take place in the same time window and are inversely related (between 500-545 m.p.f.). Quantifications were done from 3 embryos for each of L_a and L_p.

D, Plot of zippering velocities vs time (n=3) for the indicated timepoints on the x-axis (±5 mins). Note a tenfold increase in velocity mid-way through zippering (530 m.p.f.)

m.p.f. = minutes post fertilization. Error bars represent standard error of the mean (S.E.M.), The three embryo datasets used for measuring L_a values in (**C**) were used to calculate zippering velocities.

For **C** and **D**, n represents the number of AIB neurites quantified.

Fig. 4: SYG-1 and SYG-2 are required for precise placement of the AIB neurite in the anterior neighborhood

A-D, Representative confocal images of AIB (**A**) and RIM neurons (**B**) which mark the anterior neighborhood, in a wild type animal. (**C**) is a merge of **A** and **B**. The dashed

box represents the region of contact of AIB with the anterior neighborhood, magnified in (**D**). The AIB distal neurite colocalizes extensively with the anterior neighborhood in wild type animals (Arrow in **D** and Supplementary Fig. 2A,B). Cell bodies are marked with an asterisk.

E-L, As **A-D** but in the *syg-1(ky652)* (**E-H**) and *syg-2(ky671)* (**I-L**) mutant background. Note the gaps between the AIB distal neurite and the RIM neurites (**H,L**, arrows), indicating loss of contact between the AIB and the anterior neighborhood in these mutants.

M, Schematic and scatter plot of quantifications of the loss of contacts between AIB and the anterior neighborhood for wild type (n=41), *syg-1(ky652)* mutant (n=39) and s*yg-2(ky671)* animals (n=49). 'n' represents the number of AIB neurites quantified from 21, 20 and 25 animals respectively. The extent of detachment of the AIB distal neurite, and hence its deviation from the RIM neighborhood, was quantified using the indicated formula (see also Methods). Error bars indicate standard error of the mean (S.E.M.). ****p<0.0001, **p=0.0095 (one-way ANOVA with Dunnett's multiple comparisons test). n represents the number of AIB neurites quantified. Estimated effect size, d = 1.110 for WT vs. *syg-1(ky652)* and 0.775 for WT vs. *syg-2(ky671)*.

N, Quantification of the penetrance of the AIB neurite placement defect as the percentage of animals with normal AIB distal neurite placement in WT, *syg-1(ky652), syg-2(ky671), syg-1(ky652);syg-2(ky671)* double mutant, *inx-1p:syg-2* rescue, *inx-1p:syg-1* rescue and SYG-1 cosmid rescue. *inx-1p* is a cell-specific promoter driving expression in AIB (Altun et al., 2008). The green and purple bars represent *syg-1(ky652)* and *syg-2(ky671)* mutant backgrounds respectively. Numbers on bars

represent number of animals examined. ****p<0.0001 by two-sided Fisher's exact test between WT and *syg-1(ky652)*, between WT and *syg-2(ky671)*, and between *syg-1(ky652)* and SYG-1 cosmid rescue, and **p=0.0055 between *syg-2(ky671) and inx-1p:syg-2* rescue. There is no significant difference (abbreviated by n.s.) in penetrance between the *syg-1(ky652)* and *syg-1(ky652);syg-2(ky671)* (p=0.6000) populations and between *syg-1(ky652)* and the *inx-1p:syg-1* animals (p=0.3558).

Scale bar = 10 μm, applies to **A-L.**

Fig. 5: Increased local expression of SYG-1 in the anterior neighborhood coincides with zippering of the AIB neurite onto this neighborhood

A-E, Schematic (**A**) and representative confocal image of a wild type animal co-expressing (**B**) a membrane-targeted *syg-1* transcriptional reporter (see Methods, (Schwarz et al., 2009)) and (**C**) cytoplasmic AIB reporter. Merged image in (**D**). Since the *syg-1* reporter is membrane-targeted, it labels cell body outlines and neurites (**B, D**). The dashed box or inset in (**D**) represents the region of overlap between AIB and *syg-1*-expressing neurites, magnified in (**E**). Note that the *syg-1* reporter shows two bands of expression in the nerve ring (arrows in **B** and **D**) which coincide with the posterior and anterior AIB neighborhoods (orange and magenta arrows). Note also that there is no membrane outline corresponding to the AIB cell body (**B,** we drew a dashed silhouette of the AIB cell body position as determined in **C**). Asterisk indicates cell body.

F-I, As **B-E**, but with a translational SYG-1 reporter. Note the SYG-1 protein shows a similar expression pattern.

J-N, Schematic (**J**) and time-lapse images (**K-N**) of SYG-1 translational reporter expression during embryogenesis (460-640 m.p.f.). Images are deconvolved diSPIM maximum intensity projections. The dashed boxes represent the dorsal half of the nerve ring and are magnified in **O-R**. **O'-R'** are schematic diagrams representing the images in **O-R**. In (**K, O, O'**), SYG-1 expression is primarily visible in a single band containing amphid neurites, and corresponding to the AIB posterior neighborhood. The magenta dashed line and magenta arrows point to the anterior neighborhood and the orange arrow, to the posterior neighborhood. By 535 m.p.f. (**L, P, P'**), SYG-1 expression is visible in both the anterior and posterior neighborhoods. In subsequent timepoints (**M, Q, Q', N, R, R'**), SYG-1 expression increases in the anterior neighborhood and decreases in the posterior neighborhood, coincident with AIB developmental events that enable its transition from the posterior to the anterior neighborhood (Fig. 2B-K). The *syg-1* transcriptional reporter shows a similar expression pattern throughout development (Supplementary Fig. 5).

S, Plot showing relative enrichment of the *syg-1* transcriptional reporter in the anterior neighborhood over time (magenta) overlaid with plot showing percentage of the relocating AIB distal neurite that has zippered onto the anterior neighborhood (blue). Relative enrichment in the anterior neighborhood is defined as the ratio of mean intensity of the *syg-1* reporter in the band corresponding to the AIB anterior neighborhood, as compared to that in the posterior neighborhood (see Methods). This value is calculated starting at a timepoint when *syg-1* reporter expression becomes visible in the anterior neighborhood, and averaged for 4 embryos. The relative enrichment values plotted represent values calculated at the indicated developmental

1088 times on the x-axis (±10 mins). The reported values of "% AIB zippered" are averaged
1089 across the three independent embryo datasets used for the plots in Fig. 3. Note similar
1090 SYG-1 expression dynamics to zippering dynamics in AIB. Error bars represent
1091 standard error of the mean (S.E.M.).
1092 Scale bar = 10 μm, applies to **B-D**, **F-H** and **K-N**.
1093 Scale bar = 2 μm in **E, I,** and **O-R**
1094 Times are in m.p.f. (minutes post fertilization).
1095
1096 **Fig. 6: Ectopic *syg-1* expression is sufficient to alter placement of the AIB distal**
1097 **neurite**
1098
1099 **A,** Lateral view schematic of a wild type AIB neuron (cyan) in the context of the
1100 posterior (orange) and anterior (magenta) neighborhoods, and the nerve ring (light
1101 neon). Higher SYG-1 endogenous expression in the anterior neighborhood represented
1102 by yellow arrowhead.
1103 **B-C,** Confocal image of a wild type animal with AIB (labeled with cytoplasmic mCherry,
1104 in cyan) and the posterior neighborhood neurons AWC and ASE (labeled with
1105 cytoplasmic GFP, in orange). The dashed box represents the region of contact between
1106 AIB and the posterior neighborhood neurons, magnified in (**C**).
1107 **D-F,** As (**A-C**), but in the *syg-1(ky652)* lof (loss of function) mutant background. Note
1108 that the distal neurite is positioned away from the posterior neighborhood, as in wild
1109 type, although these animals display defects in fasciculation with the anterior
1110 neighborhood (as shown in Fig. 4).

G-I, As (**D-F**), but with ectopic overexpression of SYG-1 in the posterior neighborhood neurons. In the schematic (**G**), expression of SYG-1 in the posterior neighborhood (achieved here using *nphp-4p*, also see Supplementary Fig. 8A,B) is represented by a yellow arrowhead (as in (**A**), but here in posterior neighborhood). Note that the AIB distal neurite is now abnormally positioned in the posterior neighborhood in which SYG-1 was ectopically expressed (**H, I**).

J, Schematic (left) and scatter plot quantification (right) of minimum perpendicular distances (d_{min}, indicated by black double-headed arrow) between the AIB distal neurite and posterior neighborhood neurons in WT (in black, n=17), *syg-1(ky652)* (in green, n=18), and two *syg-1(ky652)* populations with SYG-1 overexpressed in two different sets of posterior neighborhood neurons via the use of *nphp-4p* and (in blue) *mgl-1bp* (in red) (n=18 and n=16 respectively). **p= 0.0056 and 0.0070 respectively (one-way ANOVA with Dunnett's multiple comparisons test). Effect size estimate, d = 1.075 and 1.140 respectively. Error bars indicate standard error of the mean (S.E.M.). n represents the number of AIB neurites quantified. Quantifications were done from 9 animals each for WT, *syg-1(ky652)* and nphp-4:syg-1; *syg-1(ky652)* and 8 animals for mgl-1b:syg-1; *syg-1(ky652)*.

K, Quantification of penetrance of the ectopic AIB neurite placement represented as the percentage of animals with the AIB distal neurite partially positioned in the posterior neighborhood in the WT, *syg-1(ky652)* and posterior SYG-1 overexpression strains (colors represent the same strains as in **J**). Numbers on bars represent number of animals examined. ***p=0.0002 for *syg-1(ky652)* and *nphp-4p* expressed SYG-1 and

****p<0.0001 for *syg-1(ky652)* and *mgl-1bp* expressed SYG-1 by two-sided Fisher's exact test.

Scale bar = 10 μm in **B**, **E** and **H** and 1 μm in **C**, **F**, and **I**. Cell body is marked with an asterisk.

Fig. 7: AIB neurite placement by retrograde zippering, and presynaptic assembly are coordinated during development

A, Axial view schematic of the AIB neurons (cyan) with presynaptic protein RAB-3 (yellow) puncta along the distal neurite. Arrowhead indicates the tip of the distal neurite and arrow/dashed line indicate the dorsal midline.

B-E, Time-lapse imaging of RAB-3 localization in AIB during embryogenesis. **B-E** are merged diSPIM maximum intensity projections of AIB labeled with membrane-tagged mCherry (cyan) and AIB presynaptic sites labeled with GFP:RAB-3 (yellow), at different timepoints during embryogenesis. **B'-E'** represent the GFP:RAB-3 channel for images in **B-E**. Note in (**B, B'**) and (**C, C'**) that the RAB-3 signal in the neurite is localized exclusively near the neurite tip. As development progresses, there is more RAB-3 signal throughout the neurite from the tip up to the midline (in (**D, D'**) and (**E, E'**)). Therefore, RAB-3 becomes progressively enriched from the tip up to the midline during development, and the timing for this process correlates, with a slight delay, with the developmental timing of AIB zippering (Fig. 2I-K). Arrowhead and arrow, as in (**A**), indicate the tip of the distal neurite and the region of the neurite near the dorsal midline (dashed vertical line) respectively. Scale bar = 10 μm applies (**B-E**) and (**B'-E'**).

F-I, Straightened distal neurites from AIB (corresponding to the region in (**B-E**) which is marked by the arrowhead (AIB tip) and arrows (dorsal midline). Note presynaptic assembly, as imaged by RAB-3 accumulation, from the tip of the neurite towards the midline of AIB, reminiscent of the zippering event (Fig. 2). Scale bar = 1 μm applies **F-I**. **J,** Schematic model showing progressive retrograde zippering leading to placement of the AIB neurite along two different layers. This is accompanied by a switch in SYG-1 expression between layers, and synaptic protein localization in a retrograde order along the neurite, resembling the order of zippering.

References

ALTUN, Z. F., CHEN, B., WANG, Z. W. & HALL, D. H. 2008. High resolution map of Caenorhabditis elegans gap junction proteins. *Developmental Dynamics*.

ARMENTI, S. T., LOHMER, L. L., SHERWOOD, D. R. & NANCE, J. 2014. Repurposing an endogenous degradation system for rapid and targeted depletion of C. elegans proteins. *Development (Cambridge)*.

AURELIO, O., BOULIN, T. & HOBERT, O. 2003. Identification of spatial and temporal cues that regulate postembryonic expression of axon maintenance factors in the C. elegans ventral nerve cord. *Development,* 130**,** 599-610.

BAIER, H. 2013. Synaptic laminae in the visual system: Molecular mechanisms forming layers of perception.

BAO, S. & CAGAN, R. 2005. Preferential adhesion mediated by Hibris and Roughest regulates morphogenesis and patterning in the Drosophila eye. *Dev Cell,* 8**,** 925-35.

BAO, S., FISCHBACH, K. F., CORBIN, V. & CAGAN, R. L. 2010. Preferential adhesion maintains separation of ommatidia in the Drosophila eye. *Dev Biol,* 344**,** 948-56.

BAO, Z., MURRAY, J. I., BOYLE, T., OOI, S. L., SANDEL, M. J. & WATERSTON, R. H. 2006. Automated cell lineage tracing in Caenorhabditis elegans. *Proceedings of the National Academy of Sciences of the United States of America*.

BARRY, J., GU, Y. & GU, C. 2010. Polarized targeting of L1-CAM regulates axonal and dendritic bundling in vitro. *European Journal of Neuroscience*.

BOYLE, T. J., BAO, Z., MURRAY, J. I., ARAYA, C. L. & WATERSTON, R. H. 2006. AceTree: a tool for visual analysis of Caenorhabditis elegans embryogenesis. *BMC Bioinformatics,* 7**,** 275.

BRITTIN, C., COOK, S., HALL, D., EMMONS, S. & COHEN, N. 2018. Volumetric reconstruction of main Caenorhabditis elegans neuropil at two different time points. *bioRxiv*.

BRITTIN, C. A., COOK, S. J., HALL, D. H., EMMONS, S. W. & COHEN, N. 2021. A multi-scale brain map derived from whole-brain volumetric reconstructions. *Nature,* 591**,** 105-110.

CANTY, L., ZAROUR, E., KASHKOOLI, L., FRANÇOIS, P. & FAGOTTO, F. 2017. Sorting at embryonic boundaries requires high heterotypic interfacial tension. *Nature Communications,* 8**,** 157.

CHAO, D. L. & SHEN, K. 2008. Functional dissection of SYG-1 and SYG-2, cell adhesion molecules required for selective synaptogenesis in C. elegans. *Mol Cell Neurosci,* 39**,** 248-57.

CHELUR, D. S. & CHALFIE, M. 2007. Targeted cell killing by reconstituted caspases. *Proc Natl Acad Sci U S A,* 104**,** 2283-8.

COOK, S. J., JARRELL, T. A., BRITTIN, C. A., WANG, Y., BLONIARZ, A. E., YAKOVLEV, M. A., NGUYEN, K. C. Q., TANG, L. T. H., BAYER, E. A., DUERR, J. S., BÜLOW, H. E., HOBERT, O., HALL, D. H. & EMMONS, S. W. 2019. Whole-animal connectomes of both Caenorhabditis elegans sexes. *Nature*.

DAVIS, M. W., HAMMARLUND, M., HARRACH, T., HULLETT, P., OLSEN, S. & JORGENSEN, E. M. 2005. Rapid single nucleotide polymophism mapping in C. elegans. *BMC Genomics*.

DEMB, J. B. & SINGER, J. H. 2012. Intrinsic properties and functional circuitry of the AII amacrine cell.

DUAN, X., KRISHNASWAMY, A., DE LA HUERTA, I. & SANES, J. R. 2014. Type II cadherins guide assembly of a direction-selective retinal circuit. *Cell,* 158**,** 793-807.

DUGUAY, D., FOTY, R. A. & STEINBERG, M. S. 2003. Cadherin-mediated cell adhesion and tissue segregation: qualitative and quantitative determinants. *Developmental Biology,* 253**,** 309-323.

DUNCAN, L. H., MOYLE, M. W., SHAO, L., SENGUPTA, T., IKEGAMI, R., KUMAR, A., GUO, M., CHRISTENSEN, R., SANTELLA, A., BAO, Z., SHROFF, H., MOHLER, W. & COLÓN-RAMOS, D. A. 2019. Isotropic light-sheet microscopy and automated cell lineage analyses to catalogue caenorhabditis elegans embryogenesis with subcellular resolution. *Journal of Visualized Experiments*.

DWORAK, H. A., CHARLES, M. A., PELLERANO, L. B. & SINK, H. 2001. Characterization of Drosophila hibris, a gene related to human nephrin. *Development,* 128**,** 4265-76.

ERZBERGER, A., JACOBO, A., DASGUPTA, A. & HUDSPETH, A. J. 2020. Mechanochemical symmetry breaking during morphogenesis of lateral-line sensory organs. *Nat Phys,* 16**,** 949-957.

FORNITO, A., ZALESKY, A. & BULLMORE, E. T. 2016. *Fundamentals of brain network analysis,* Amsterdam ; Boston, Elsevier/Academic Press.

FOTY, R. A., PFLEGER, C. M., FORGACS, G. & STEINBERG, M. S. 1996. Surface tensions of embryonic tissues predict their mutual envelopment behavior. *Development,* 122**,** 1611-1620.

FOTY, R. A. & STEINBERG, M. S. 2005. The differential adhesion hypothesis: A direct evaluation. *Developmental Biology*.

FOTY, R. A. & STEINBERG, M. S. 2013. Differential adhesion in model systems.

GABRIEL, JENS P., TRIVEDI, CHINTAN A., MAURER, COLETTE M., RYU, S. & BOLLMANN, JOHANN H. 2012. Layer-Specific Targeting of Direction-Selective Neurons in the Zebrafish Optic Tectum. *Neuron,* 76**,** 1147-1160.

GALLETTA, B. J., CHAKRAVARTI, M., BANERJEE, R. & ABMAYR, S. M. 2004. SNS: Adhesive properties, localization requirements and ectodomain dependence in S2 cells and embryonic myoblasts. *Mech Dev,* 121**,** 1455-68.

GARG, P., VERMA, R., NIHALANI, D., JOHNSTONE, D. B. & HOLZMAN, L. B. 2007. Neph1 Cooperates with Nephrin To Transduce a Signal That Induces Actin Polymerization. *Molecular and Cellular Biology*.

GERKE, P., HUBER, T. B., SELLIN, L., BENZING, T. & WALZ, G. 2003. Homodimerization and heterodimerization of the glomerular podocyte proteins nephrin and NEPH1. *J Am Soc Nephrol,* 14**,** 918-26.

GODT, D. & TEPASS, U. 1998. Drosophila oocyte localization is mediated by differential cadherin-based adhesion. *Nature,* 395**,** 387-391.

GONZALEZ-REYES, A. & ST JOHNSTON, D. 1998. The Drosophila AP axis is polarised by the cadherin-mediated positioning of the oocyte. *Development,* 125**,** 3635-3644.

GREER, E. R., PEREZ, C. L., VAN GILST, M. R., LEE, B. H. & ASHRAFI, K. 2008. Neural and molecular dissection of a C. elegans sensory circuit that regulates fat and feeding. *Cell Metab,* 8**,** 118-31.

HAN, J., KAMBER, M. & PEI, J. 2012. 2 - Getting to Know Your Data. *In:* HAN, J., KAMBER, M. & PEI, J. (eds.) *Data Mining (Third Edition).* Boston: Morgan Kaufmann.

JONTES, J. D., BUCHANAN, J. & SMITH, S. J. 2000. Growth cone and dendrite dynamics in zebrafish embryos: early events in synaptogenesis imaged in vivo. *Nat Neurosci,* 3**,** 231-7.

KATZ, M. J. 1985. How straight do axons grow? *The Journal of Neuroscience,* 5**,** 589.

KIM, B. & EMMONS, S. W. 2017. Multiple conserved cell adhesion protein interactions mediate neural wiring of a sensory circuit in C. elegans. *Elife,* 6.

KIM, K., KIM, R. & SENGUPTA, P. 2010. The HMX/NKX homeodomain protein MLS-2 specifies the identity of the AWC sensory neuron type via regulation of the ceh-36 Otx gene in C. elegans. *Development,* 137**,** 963-74.

KOESTINGER, G., MARTIN, K. A. C., ROTH, S. & RUSCH, E. S. 2017. Synaptic connections formed by patchy projections of pyramidal cells in the superficial layers of cat visual cortex. *Brain Struct Funct,* 222**,** 3025-3042.

KOLB, H. 1995. *Roles of Amacrine Cells*.

KOLODKIN, A. L. & HIESINGER, P. R. 2017. Wiring visual systems: common and divergent mechanisms and principles. *Curr Opin Neurobiol,* 42**,** 128-135.

KRIEG, M., ARBOLEDA-ESTUDILLO, Y., PUECH, P. H., KAFER, J., GRANER, F., MULLER, D. J. & HEISENBERG, C. P. 2008. Tensile forces govern germ-layer organization in zebrafish. *Nat Cell Biol,* 10**,** 429-36.

KUMAR, A., WU, Y., CHRISTENSEN, R., CHANDRIS, P., GANDLER, W., MCCREEDY, E., BOKINSKY, A., COLÓN-RAMOS, D. A., BAO, Z., MCAULIFFE,

M., RONDEAU, G. & SHROFF, H. 2014. Dual-view plane illumination microscopy for rapid and spatially isotropic imaging. *Nature Protocols*.

KUNZEVITZKY, N. J., WILLEFORD, K. T., FEUER, W. J., ALMEIDA, M. V. & GOLDBERG, J. L. 2013. Amacrine cell subtypes differ in their intrinsic neurite growth capacity. *Investigative Ophthalmology and Visual Science*.

KURAMOCHI, M. & DOI, M. 2019. An Excitatory/Inhibitory Switch From Asymmetric Sensory Neurons Defines Postsynaptic Tuning for a Rapid Response to NaCl in Caenorhabditis elegans. *Frontiers in Molecular Neuroscience,* 11**,** 484.

LIN, D. M., FETTER, R. D., KOPCZYNSKI, C., GRENNINGLOH, G. & GOODMAN, C. S. 1994. Genetic analysis of Fasciclin II in Drosophila: defasciculation, refasciculation, and altered fasciculation. *Neuron,* 13**,** 1055-69.

MARC, R. E., ANDERSON, J. R., JONES, B. W., SIGULINSKY, C. L. & LAURITZEN, J. S. 2014. The AII amacrine cell connectome: a dense network hub. *Front Neural Circuits,* 8**,** 104.

MAYNARD, D. M. 1962. Organization of Neuropil. *Am. Zoologist***,** 79-96.

MELLO, C. & FIRE, A. 1995. DNA Transformation. *Methods in Cell Biology*.

MILLARD, S. S. & PECOT, M. Y. 2018. Strategies for assembling columns and layers in the Drosophila visual system. *Neural Dev,* 13**,** 11.

MINEVICH, G., PARK, D. S., BLANKENBERG, D., POOLE, R. J. & HOBERT, O. 2012. CloudMap: A cloud-based pipeline for analysis of mutant genome sequences. *Genetics*.

MISSAIRE, M. & HINDGES, R. 2015. The role of cell adhesion molecules in visual circuit formation: from neurite outgrowth to maps and synaptic specificity. *Dev Neurobiol,* 75**,** 569-83.

MISSLER, M., SUDHOF, T. C. & BIEDERER, T. 2012. Synaptic cell adhesion. *Cold Spring Harb Perspect Biol,* 4**,** a005694.

MOYLE, M. W., BARNES, K. M., KUCHROO, M., GONOPOLSKIY, A., DUNCAN, L. H., SENGUPTA, T., SHAO, L., GUO, M., SANTELLA, A., CHRISTENSEN, R., KUMAR, A., WU, Y., MOON, K. R., WOLF, G., KRISHNASWAMY, S., BAO, Z., SHROFF, H., MOHLER, W. A. & COLON-RAMOS, D. A. 2021. Structural and developmental principles of neuropil assembly in C. elegans. *Nature,* 591**,** 99-104.

MURRAY, J. I., BAO, Z., BOYLE, T. J. & WATERSTON, R. H. 2006. The lineaging of fluorescently-labeled Caenorhabditis elegans embryos with StarryNite and AceTree. *Nat Protoc,* 1**,** 1468-76.

NEUMANN-HAEFELIN, E., KRAMER-ZUCKER, A., SLANCHEV, K., HARTLEBEN, B., NOUTSOU, F., MARTIN, K., WANNER, N., RITTER, A., GODEL, M., PAGEL, P., FU, X., MULLER, A., BAUMEISTER, R., WALZ, G. & HUBER, T. B. 2010. A model organism approach: defining the role of Neph proteins as regulators of neuron and kidney morphogenesis. *Hum Mol Genet,* 19**,** 2347-59.

NEVIN, L. M., TAYLOR, M. R. & BAIER, H. 2008. Hardwiring of fine synaptic layers in the zebrafish visual pathway. *Neural Development*.

NGUYEN-BA-CHARVET, K. T. & CHEDOTAL, A. 2014. Development of retinal layers. *C R Biol,* 337**,** 153-9.

OZKAN, E., CHIA, P. H., WANG, R. R., GORIATCHEVA, N., BOREK, D., OTWINOWSKI, Z., WALZ, T., SHEN, K. & GARCIA, K. C. 2014. Extracellular

architecture of the SYG-1/SYG-2 adhesion complex instructs synaptogenesis. *Cell,* 156**,** 482-94.

OZTOKATLI, H., HORNBERG, M., BERGHARD, A. & BOHM, S. 2012. Retinoic acid receptor and CNGA2 channel signaling are part of a regulatory feedback loop controlling axonal convergence and survival of olfactory sensory neurons. *FASEB J,* 26**,** 617-27.

PACKER, J. S., ZHU, Q., HUYNH, C., SIVARAMAKRISHNAN, P., PRESTON, E., DUECK, H., STEFANIK, D., TAN, K., TRAPNELL, C., KIM, J., WATERSTON, R. H. & MURRAY, J. I. 2019. A lineage-resolved molecular atlas of C. elegans embryogenesis at single-cell resolution. *Science,* 365.

PETROVIC, M. & HUMMEL, T. 2008. Temporal identity in axonal target layer recognition. *Nature*.

PIGGOTT, B. J., LIU, J., FENG, Z., WESCOTT, S. A. & XU, X. Z. S. 2011. The neural circuits and synaptic mechanisms underlying motor initiation in C. elegans. *Cell*.

POSKANZER, K., NEEDLEMAN, L. A., BOZDAGI, O. & HUNTLEY, G. W. 2003. N-cadherin regulates ingrowth and laminar targeting of thalamocortical axons. *The Journal of neuroscience : the official journal of the Society for Neuroscience*.

PRICE, S. R., DE MARCO GARCIA, N. V., RANSCHT, B. & JESSELL, T. M. 2002. Regulation of motor neuron pool sorting by differential expression of type II cadherins. *Cell,* 109**,** 205-16.

ROBLES, E., FILOSA, A. & BAIER, H. 2013. Precise lamination of retinal axons generates multiple parallel input pathways in the tectum. *Journal of Neuroscience*.

RUBINOV, M. & SPORNS, O. 2010. Complex network measures of brain connectivity: Uses and interpretations. *NeuroImage*.

SABRIN, K., WEI, Y., VAN DEN HEUVEL, M. & DOVROLIS, C. 2019. The hourglass organization of the Caenorhabditis elegans connectome. *bioRxiv*.

SANES, J. R. & ZIPURSKY, S. L. 2010. Design principles of insect and vertebrate visual systems. *Neuron,* 66**,** 15-36.

SANES, J. R. & ZIPURSKY, S. L. 2020. Synaptic Specificity, Recognition Molecules, and Assembly of Neural Circuits.

SARIN, S., PRABHU, S., O'MEARA, M. M., PE'ER, I. & HOBERT, O. 2008. Caenorhabditis elegans mutant allele identification by whole-genome sequencing. *Nature Methods*.

SCHINDELIN, J., ARGANDA-CARRERAS, I., FRISE, E., KAYNIG, V., LONGAIR, M., PIETZSCH, T., PREIBISCH, S., RUEDEN, C., SAALFELD, S., SCHMID, B., TINEVEZ, J. Y., WHITE, D. J., HARTENSTEIN, V., ELICEIRI, K., TOMANCAK, P. & CARDONA, A. 2012. Fiji: an open-source platform for biological-image analysis. *Nat Methods,* 9**,** 676-82.

SCHOTZ, E. M., BURDINE, R. D., JULICHER, F., STEINBERG, M. S., HEISENBERG, C. P. & FOTY, R. A. 2008. Quantitative differences in tissue surface tension influence zebrafish germ layer positioning. *HFSP J,* 2**,** 42-56.

SCHÜRMANN, F. W. 2016. Fine structure of synaptic sites and circuits in mushroom bodies of insect brains.

SCHWABE, T., BORYCZ, J. A., MEINERTZHAGEN, I. A. & CLANDININ, T. R. 2019. Differential Adhesion Determines the Organization of Synaptic Fascicles in the Drosophila Visual System. *Curr Biol,* 29**,** 715.

SCHWARZ, V., PAN, J., VOLTMER-IRSCH, S. & HUTTER, H. 2009. IgCAMs redundantly control axon navigation in Caenorhabditis elegans. *Neural Development*.

SERIZAWA, S., MIYAMICHI, K., TAKEUCHI, H., YAMAGISHI, Y., SUZUKI, M. & SAKANO, H. 2006. A Neuronal Identity Code for the Odorant Receptor-Specific and Activity-Dependent Axon Sorting. *Cell*.

SHAH, P. K., TANNER, M. R., KOVACEVIC, I., RANKIN, A., MARSHALL, T. E., NOBLETT, N., TRAN, N. N., ROENSPIES, T., HUNG, J., CHEN, Z., SLATCULESCU, C., PERKINS, T. J., BAO, Z. & COLAVITA, A. 2017. PCP and SAX-3/Robo Pathways Cooperate to Regulate Convergent Extension-Based Nerve Cord Assembly in C. elegans. *Developmental cell,* 41**,** 195-203.e3.

SHEN, K. & BARGMANN, C. I. 2003. The immunoglobulin superfamily protein SYG-1 determines the location of specific synapses in C. elegans. *Cell,* 112**,** 619-30.

SHEN, K., FETTER, R. D. & BARGMANN, C. I. 2004. Synaptic specificity is generated by the synaptic guidepost protein SYG-2 and its receptor, SYG-1. *Cell*.

SMIT, D., FOUQUET, C., PINCET, F., ZAPOTOCKY, M. & TREMBLEAU, A. 2017. Axon tension regulates fasciculation/defasciculation through the control of axon shaft zippering. *Elife,* 6.

SOIZA-REILLY, M. & COMMONS, K. G. 2014. Unraveling the architecture of the dorsal raphe synaptic neuropil using high-resolution neuroanatomy. *Front Neural Circuits,* 8**,** 105.

STEINBERG, M. S. 1962. Mechanism of tissue reconstruction by dissociated cells, II: Time-course of events. *Science*.

STEINBERG, M. S. 1963. Reconstruction of tissues by dissociated cells. Some morphogenetic tissue movements and the sorting out of embryonic cells may have a common explanation. *Science,* 141**,** 401-8.

STEINBERG, M. S. 1970. Does differential adhesion govern self-assembly processes in histogenesis? Equilibrium configurations and the emergence of a hierarchy among populations of embryonic cells. *Journal of Experimental Zoology,* 173**,** 395-433.

STEINBERG, M. S. & GILBERT, S. F. 2004. Townes and Holtfreter (1955): directed movements and selective adhesion of embryonic amphibian cells. *J Exp Zool A Comp Exp Biol,* 301**,** 701-6.

STEINBERG, M. S. & TAKEICHI, M. 1994. Experimental specification of cell sorting, tissue spreading, and specific spatial patterning by quantitative differences in cadherin expression. *Proc Natl Acad Sci U S A,* 91**,** 206-9.

STRETTOI, E., RAVIOLA, E. & DACHEUX, R. F. 1992. Synaptic connections of the narrow-field, bistratified rod amacrine cell (AII) in the rabbit retina. *Journal of Comparative Neurology*.

STRUNKELNBERG, M., BONENGEL, B., MODA, L. M., HERTENSTEIN, A., DE COUET, H. G., RAMOS, R. G. & FISCHBACH, K. F. 2001. rst and its paralogue kirre act redundantly during embryonic muscle development in Drosophila. *Development,* 128**,** 4229-39.

1418 TAN, L., ZHANG, K. X., PECOT, M. Y., NAGARKAR-JAISWAL, S., LEE, P. T.,
1419 TAKEMURA, S. Y., MCEWEN, J. M., NERN, A., XU, S., TADROS, W., CHEN,
1420 Z., ZINN, K., BELLEN, H. J., MOREY, M. & ZIPURSKY, S. L. 2015. Ig
1421 Superfamily Ligand and Receptor Pairs Expressed in Synaptic Partners in
1422 Drosophila. *Cell*.
1423 TAYLOR, W. R. & SMITH, R. G. 2012. The role of starburst amacrine cells in visual
1424 signal processing. *Visual Neuroscience*.
1425 TESSIER-LAVIGNE, M. & GOODMAN, C. S. 1996. The molecular biology of axon
1426 guidance. *Science,* 274**,** 1123-33.
1427 TOWLSON, E. K., VÉRTES, P. E., AHNERT, S. E., SCHAFER, W. R. & BULLMORE,
1428 E. T. 2013. The rich club of the C. elegans neuronal connectome. *Journal of*
1429 *Neuroscience*.
1430 VOYIADJIS, A. G., DOUMI, M., CURCIO, E. & SHINBROT, T. 2011. Fasciculation and
1431 defasciculation of neurite bundles on micropatterned substrates. *Annals of*
1432 *Biomedical Engineering*.
1433 WEIGERT, M., SCHMIDT, U., BOOTHE, T., MÜLLER, A., DIBROV, A., JAIN, A.,
1434 WILHELM, B., SCHMIDT, D., BROADDUS, C., CULLEY, S., ROCHA-MARTINS,
1435 M., SEGOVIA-MIRANDA, F., NORDEN, C., HENRIQUES, R., ZERIAL, M.,
1436 SOLIMENA, M., RINK, J., TOMANCAK, P., ROYER, L., JUG, F. & MYERS, E.
1437 W. 2018. Content-aware image restoration: pushing the limits of fluorescence
1438 microscopy. *Nature Methods*.
1439 WHITE, J. G., SOUTHGATE, E., THOMSON, J. N. & BRENNER, S. 1983. Factors that
1440 determine connectivity in the nervous system of Caenorhabditis elegans. *Cold*
1441 *Spring Harbor symposia on quantitative biology*.
1442 WHITE, J. G., SOUTHGATE, E., THOMSON, J. N. & BRENNER, S. 1986. The
1443 structure of the nervous system of the nematode Caenorhabditis elegans. *Philos*
1444 *Trans R Soc Lond B Biol Sci,* 314**,** 1-340.
1445 WITVLIET, D., MULCAHY, B., MITCHELL, J. K., MEIROVITCH, Y., BERGER, D. R.,
1446 WU, Y., LIU, Y., KOH, W. X., PARVATHALA, R., HOLMYARD, D., SCHALEK, R.
1447 L., SHAVIT, N., CHISHOLM, A. D., LICHTMAN, J. W., SAMUEL, A. D. T. &
1448 ZHEN, M. 2020. Connectomes across development reveal principles of brain
1449 maturation in C. elegans. *bioRxiv***,** 2020.04.30.066209-2020.04.30.066209.
1450 WU, Y., CHANDRIS, P., WINTER, P. W., KIM, E. Y., JAUMOUILLÉ, V., KUMAR, A.,
1451 GUO, M., LEUNG, J. M., SMITH, C., REY-SUAREZ, I., LIU, H., WATERMAN, C.
1452 M., RAMAMURTHI, K. S., LA RIVIERE, P. J. & SHROFF, H. 2016. Simultaneous
1453 multiview capture and fusion improves spatial resolution in wide-field and light-
1454 sheet microscopy. *Optica*.
1455 WU, Y., GHITANI, A., CHRISTENSEN, R., SANTELLA, A., DU, Z., RONDEAU, G.,
1456 BAO, Z., COLON-RAMOS, D. & SHROFF, H. 2011. Inverted selective plane
1457 illumination microscopy (iSPIM) enables coupled cell identity lineaging and
1458 neurodevelopmental imaging in Caenorhabditis elegans. *Proc Natl Acad Sci U S*
1459 *A,* 108**,** 17708-13.
1460 WU, Y., WAWRZUSIN, P., SENSENEY, J., FISCHER, R. S., CHRISTENSEN, R.,
1461 SANTELLA, A., YORK, A. G., WINTER, P. W., WATERMAN, C. M., BAO, Z.,
1462 COLÓN-RAMOS, D. A., MCAULIFFE, M. & SHROFF, H. 2013. Spatially isotropic

four-dimensional imaging with dual-view plane illumination microscopy. *Nature Biotechnology*.

XIE, X., TABUCHI, M., BROWN, M. P., MITCHELL, S. P., WU, M. N. & KOLODKIN, A. L. 2017. The laminar organization of the Drosophila ellipsoid body is semaphorin-dependent and prevents the formation of ectopic synaptic connections. *Elife,* 6.

XU, C. S., JANUSZEWSKI, M., LU, Z., TAKEMURA, S.-Y., HAYWORTH, K. J., HUANG, G., SHINOMIYA, K., MAITIN-SHEPARD, J., ACKERMAN, D., BERG, S., BLAKELY, T., BOGOVIC, J., CLEMENTS, J., DOLAFI, T., HUBBARD, P., KAINMUELLER, D., KATZ, W., KAWASE, T., KHAIRY, K. A., LEAVITT, L., LI, P. H., LINDSEY, L., NEUBARTH, N., OLBRIS, D. J., OTSUNA, H., TROUTMAN, E. T., UMAYAM, L., ZHAO, T., ITO, M., GOLDAMMER, J., WOLFF, T., SVIRSKAS, R., SCHLEGEL, P., NEACE, E. R., KNECHT, C. J., ALVARADO, C. X., BAILEY, D. A., BALLINGER, S., BORYCZ, J. A., CANINO, B. S., CHEATHAM, N., COOK, M., DREHER, M., DUCLOS, O., EUBANKS, B., FAIRBANKS, K., FINLEY, S., FORKNALL, N., FRANCIS, A., HOPKINS, G. P., JOYCE, E. M., KIM, S., KIRK, N. A., KOVALYAK, J., LAUCHIE, S. A., LOHFF, A., MALDONADO, C., MANLEY, E. A., MCLIN, S., MOONEY, C., NDAMA, M., OGUNDEYI, O., OKEOMA, N., ORDISH, C., PADILLA, N., PATRICK, C., PATERSON, T., PHILLIPS, E. E., PHILLIPS, E. M., RAMPALLY, N., RIBEIRO, C., ROBERTSON, M. K., RYMER, J. T., RYAN, S. M., SAMMONS, M., SCOTT, A. K., SCOTT, A. L., SHINOMIYA, A., SMITH, C., SMITH, K., SMITH, N. L., SOBESKI, M. A., SULEIMAN, A., SWIFT, J., TAKEMURA, S., TALEBI, I., TARNOGORSKA, D., TENSHAW, E., TOKHI, T., WALSH, J. J., YANG, T., HORNE, J. A., LI, F., PAREKH, R., RIVLIN, P. K., JAYARAMAN, V., ITO, K., SAALFELD, S., GEORGE, R., MEINERTZHAGEN, I., et al. 2020. A Connectome of the Adult Drosophila Central Brain. *bioRxiv***,** 2020.01.21.911859-2020.01.21.911859.

YAMAGATA, M. & SANES, J. R. 2008. Dscam and Sidekick proteins direct lamina-specific synaptic connections in vertebrate retina. *Nature*.

YAMAGATA, M. & SANES, J. R. 2012. Expanding the Ig superfamily code for laminar specificity in retina: Expression and role of contactins. *Journal of Neuroscience*.

YIP, Z. C. & HEIMAN, M. G. 2018. Ordered arrangement of dendrites within a C. elegans sensory nerve bundle. *Elife,* 7.

ZHENG, Z., LAURITZEN, J. S., PERLMAN, E., ROBINSON, C. G., NICHOLS, M., MILKIE, D., TORRENS, O., PRICE, J., FISHER, C. B., SHARIFI, N., CALLE-SCHULER, S. A., KMECOVA, L., ALI, I. J., KARSH, B., TRAUTMAN, E. T., BOGOVIC, J. A., HANSLOVSKY, P., JEFFERIS, G. S. X. E., KAZHDAN, M., KHAIRY, K., SAALFELD, S., FETTER, R. D. & BOCK, D. D. 2018. A Complete Electron Microscopy Volume of the Brain of Adult Drosophila melanogaster. *Cell,* 174**,** 730-743.e22.

Fig 1

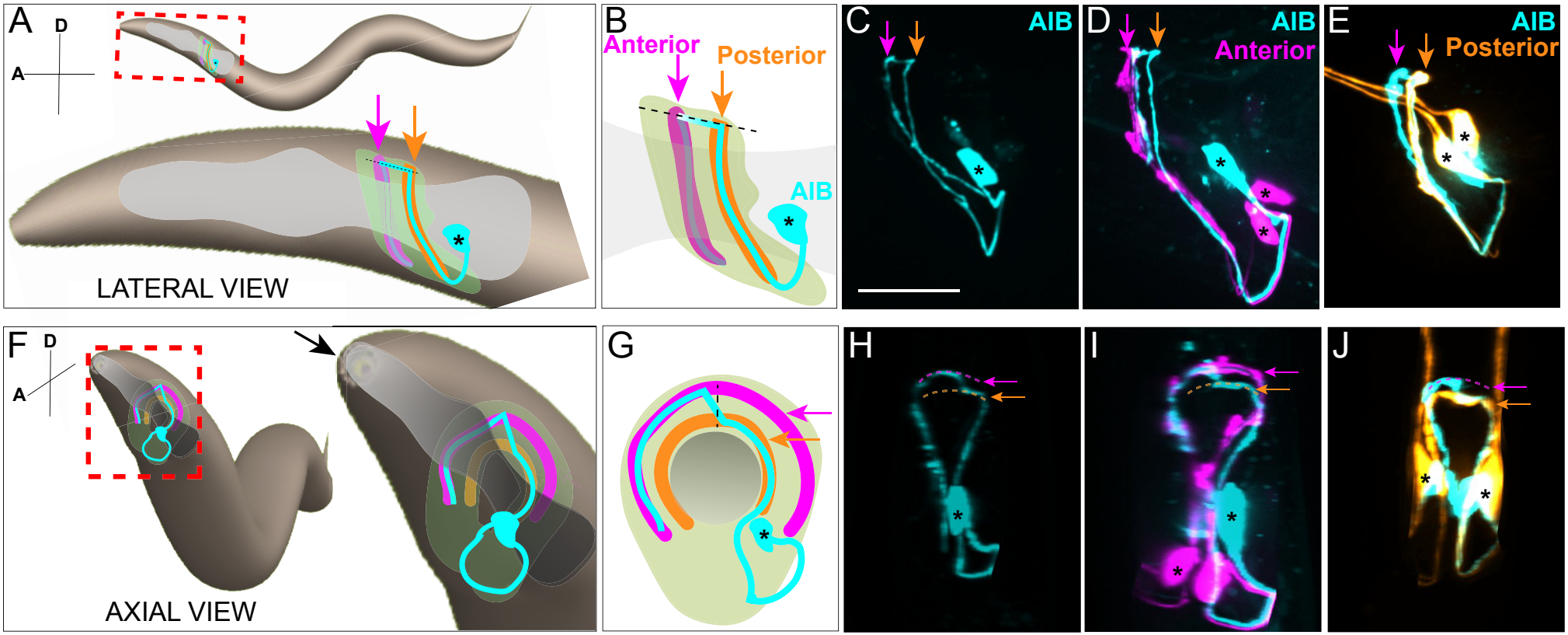
A
D
A
LATERAL VIEW
B
Anterior
Posterior
AIB
C
AIB
D
AIB
Anterior
E
AIB
Posterior
F
D
A
AXIAL VIEW
G
H
I
J
LATERAL VIEW
AXIAL VIEW
K
AIBL
L
AIBL
S2
S3
M
AIBL
AIBR
N
AIBL
AIBR
Posterior
Anterior

Fig 2

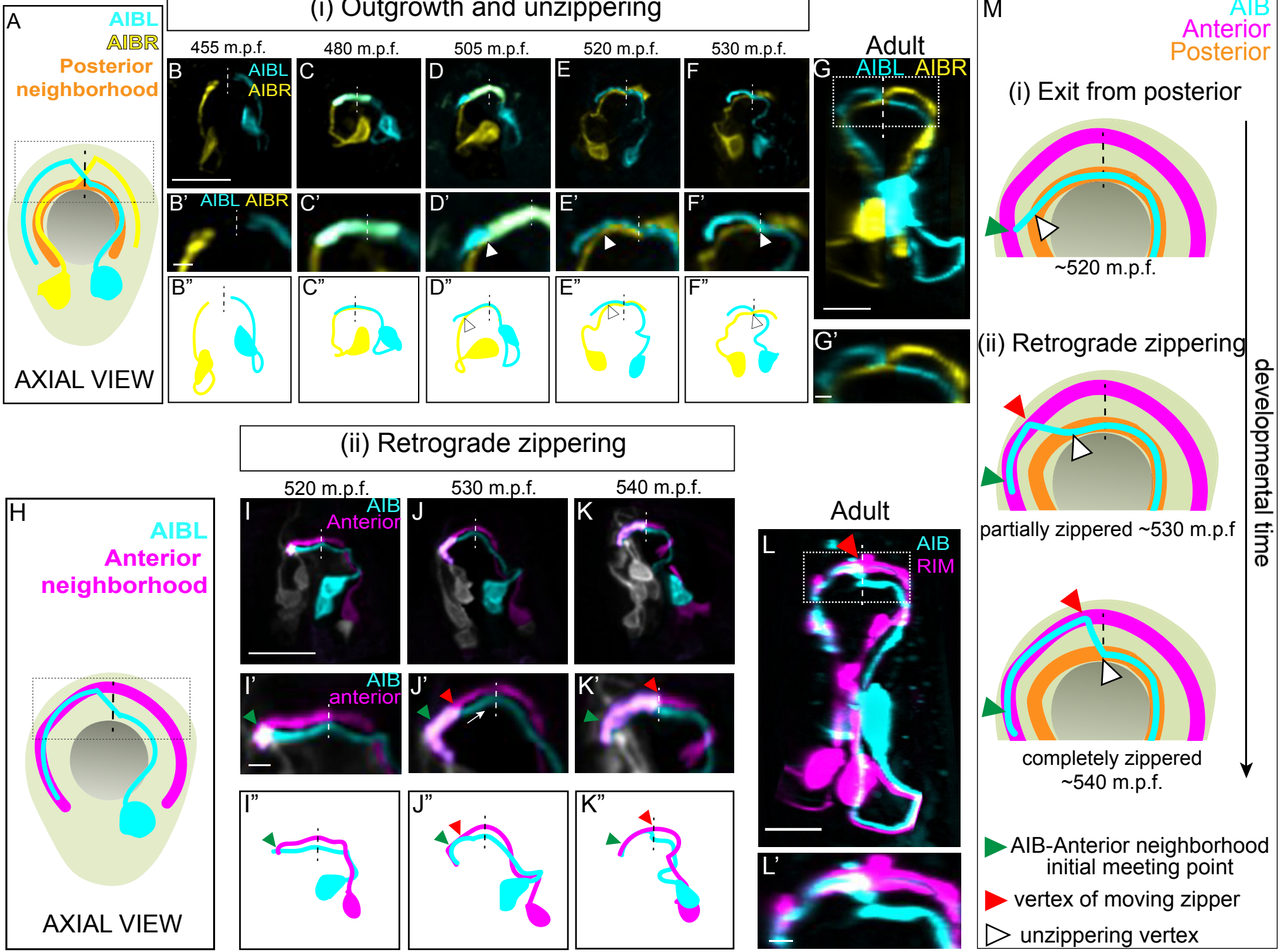
A
AIBL
AIBR
Posterior neighborhood
AXIAL VIEW
(i) Outgrowth and unzippering
455 m.p.f.
480 m.p.f.
505 m.p.f.
520 m.p.f.
530 m.p.f.
Adult
B AIBL AIBR
C
D
E
F
G AIBL AIBR
B' AIBL AIBR
C'
D'
E'
F'
G'
B"
C"
D"
E"
F"
M
AIB
Anterior
Posterior
(i) Exit from posterior
~520 m.p.f.
(ii) Retrograde zippering
partially zippered ~530 m.p.f
completely zippered ~540 m.p.f.
developmental time
AIB-Anterior neighborhood initial meeting point
vertex of moving zipper
unzippering vertex
(ii) Retrograde zippering
520 m.p.f.
530 m.p.f.
540 m.p.f.
H
AIBL
Anterior neighborhood
AXIAL VIEW
I AIB Anterior
J
K
I' AIB anterior
J'
K'
I"
J"
K"
Adult
L AIB RIM
L'

Fig 3

A

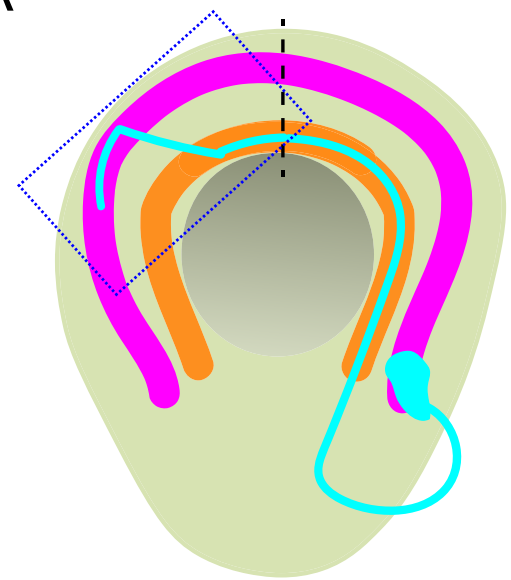

AXIAL VIEW

B

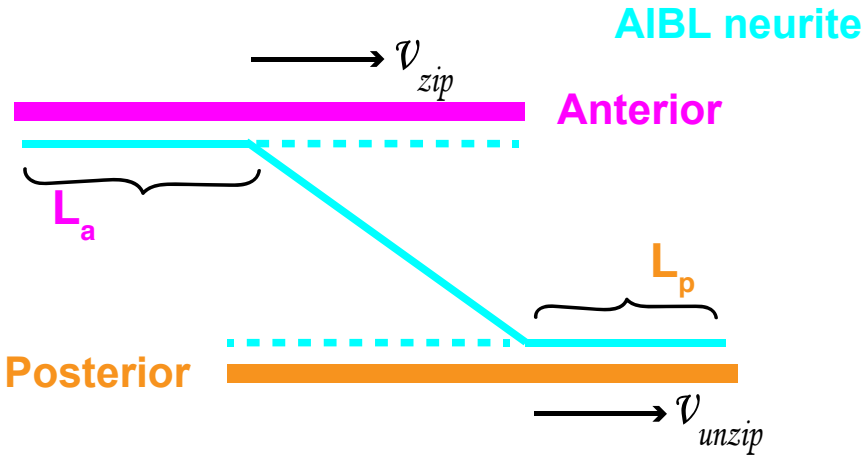

B'

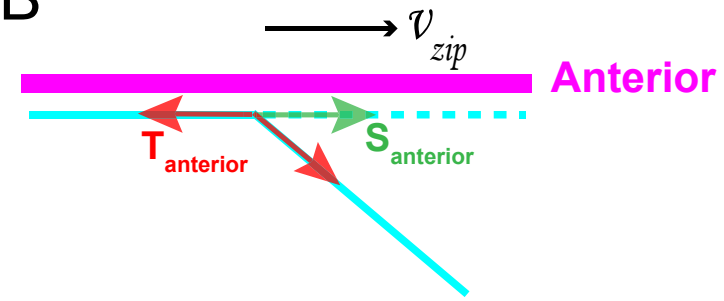

C

AIB neurite position in Anterior/Posterior neighborhoods

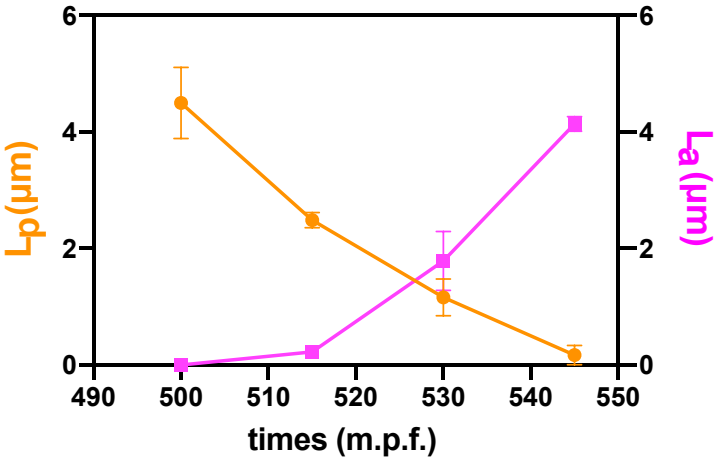

D

Zippering velocities

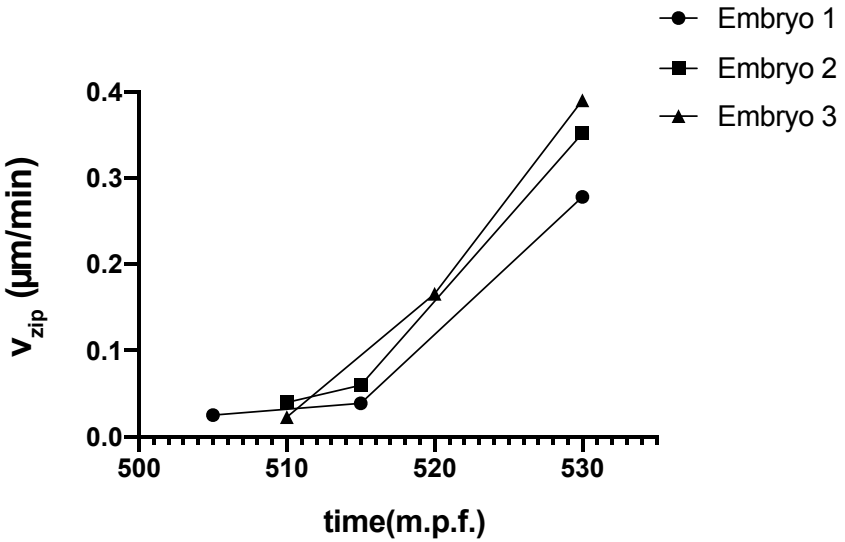

Fig 4

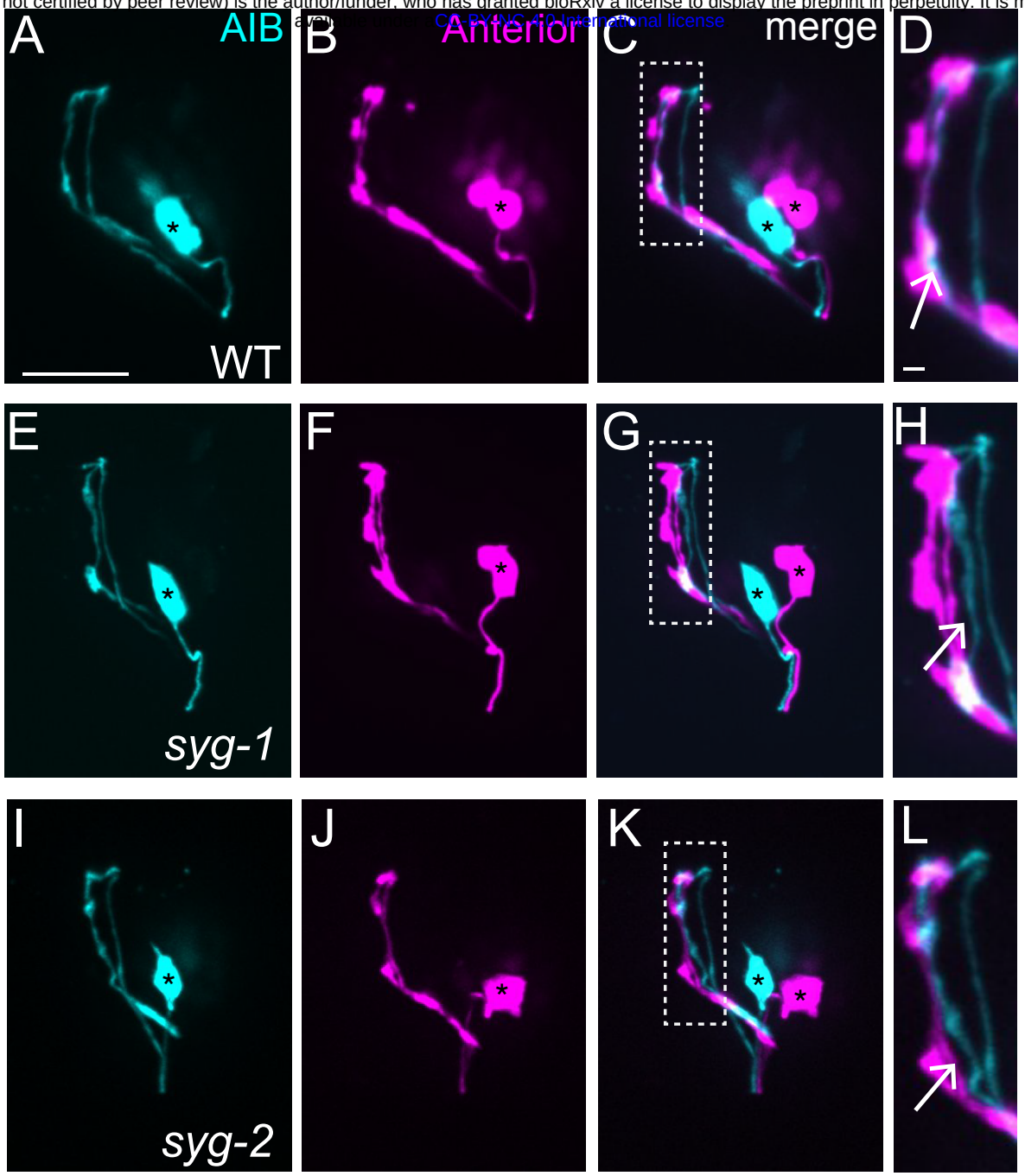

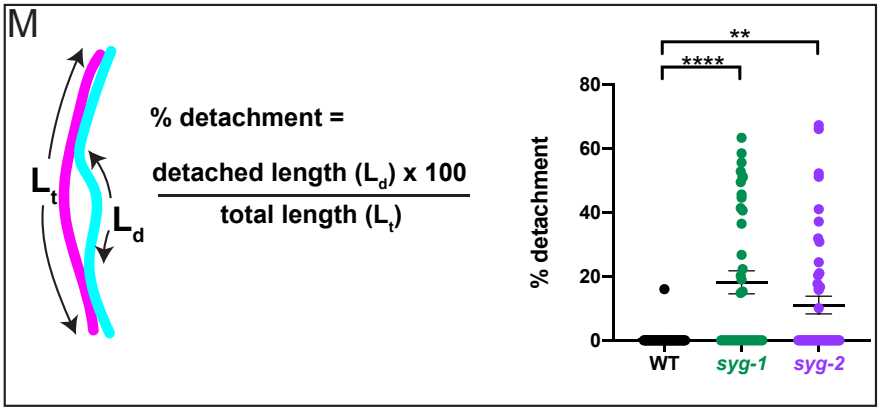

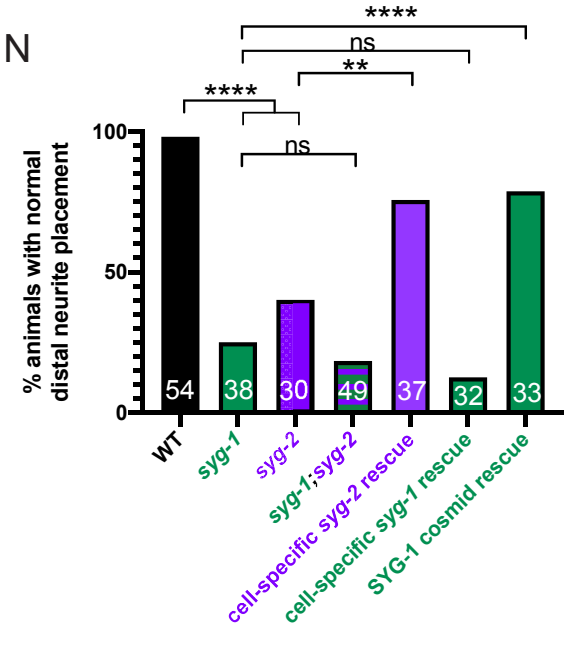

Fig 5

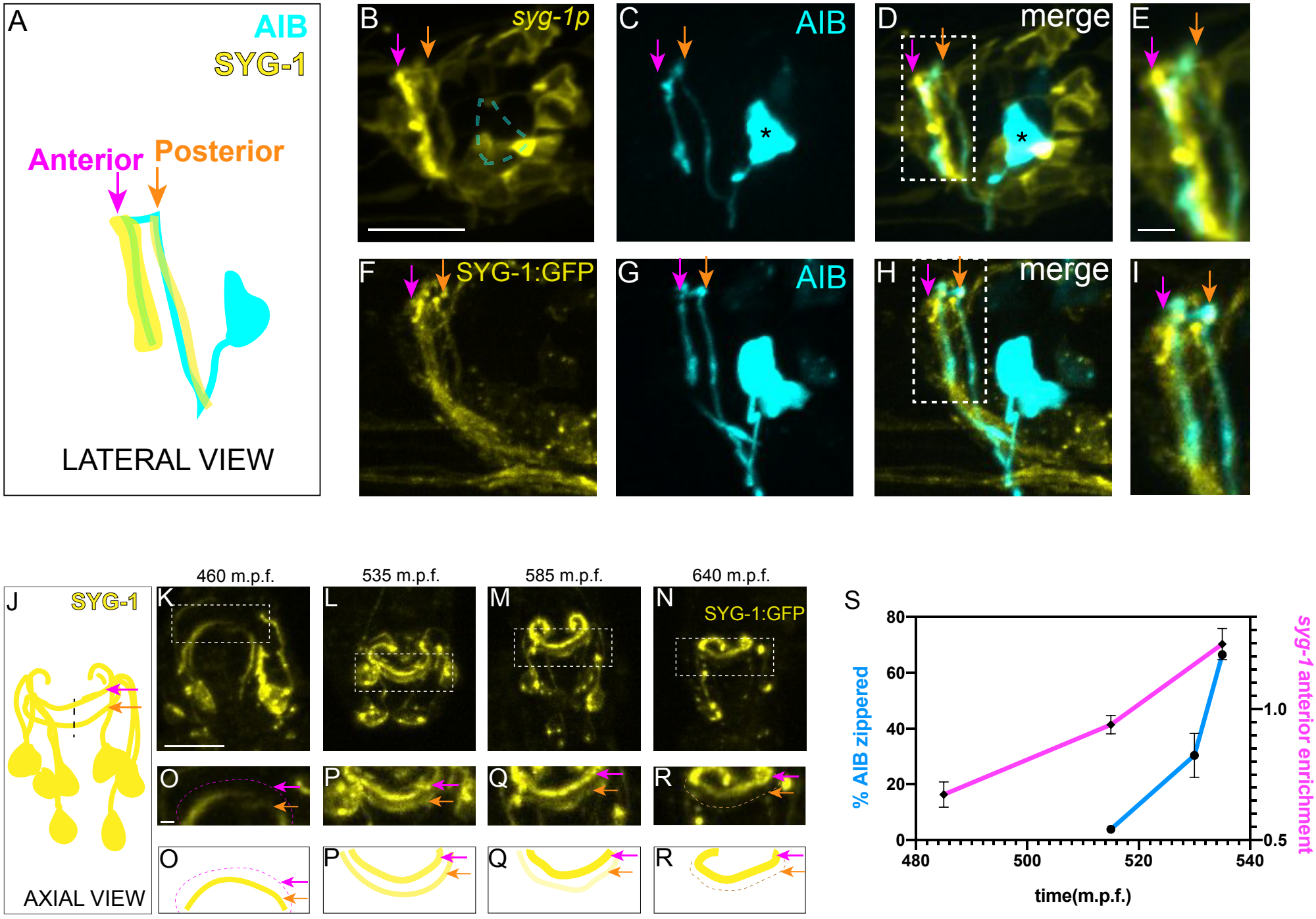
A
AIB
SYG-1
Anterior
Posterior
LATERAL VIEW
B
syg-1p
C
AIB
D
merge
E
F
SYG-1:GFP
G
AIB
H
merge
I
J
SYG-1
AXIAL VIEW
460 m.p.f.
535 m.p.f.
585 m.p.f.
640 m.p.f.
K
L
M
N
SYG-1:GFP
O
P
Q
R
S
% AIB zippered
syg-1 anterior enrichment
time(m.p.f.)
0
20
40
60
80
0.5
1.0
480
500
520
540

Fig 6

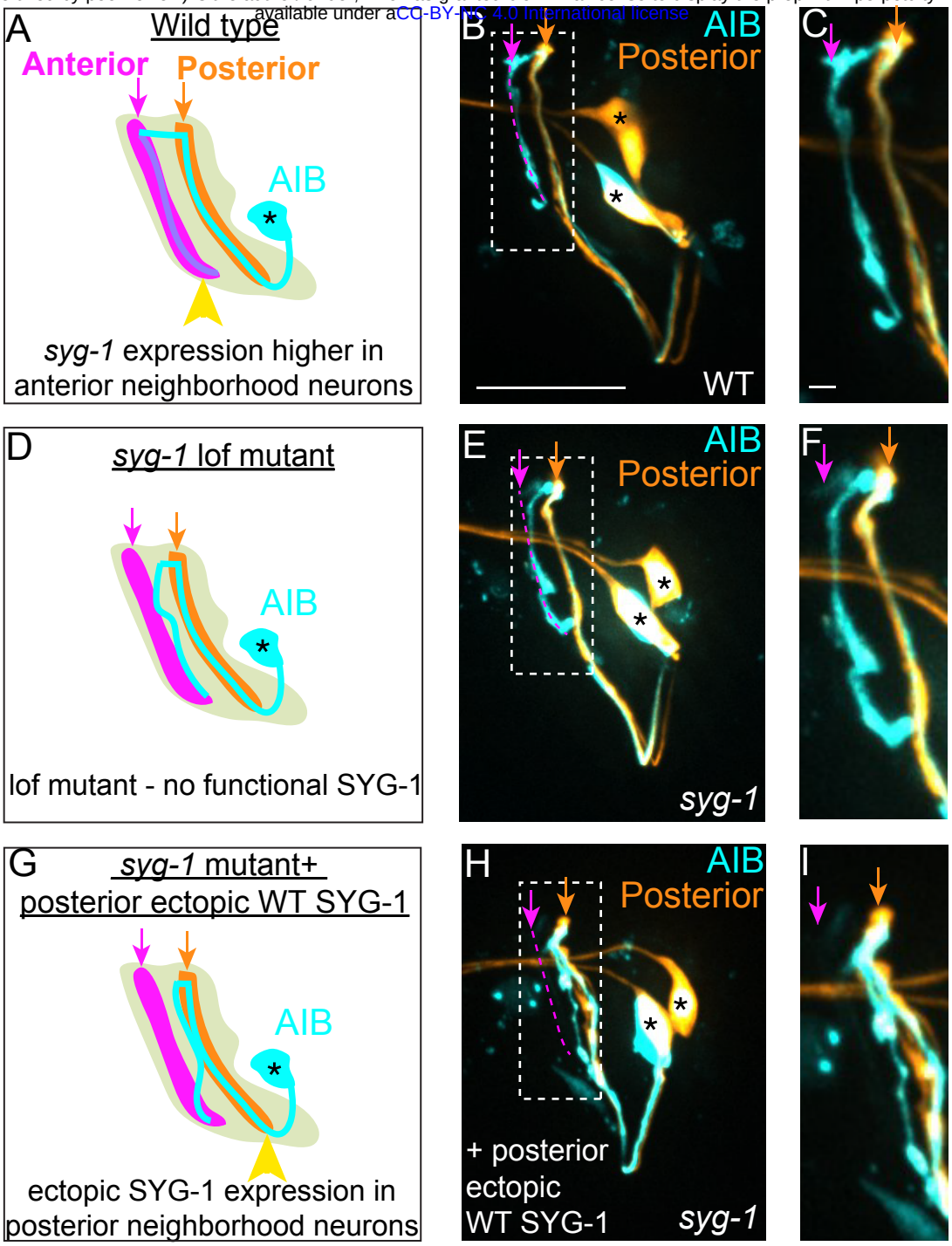

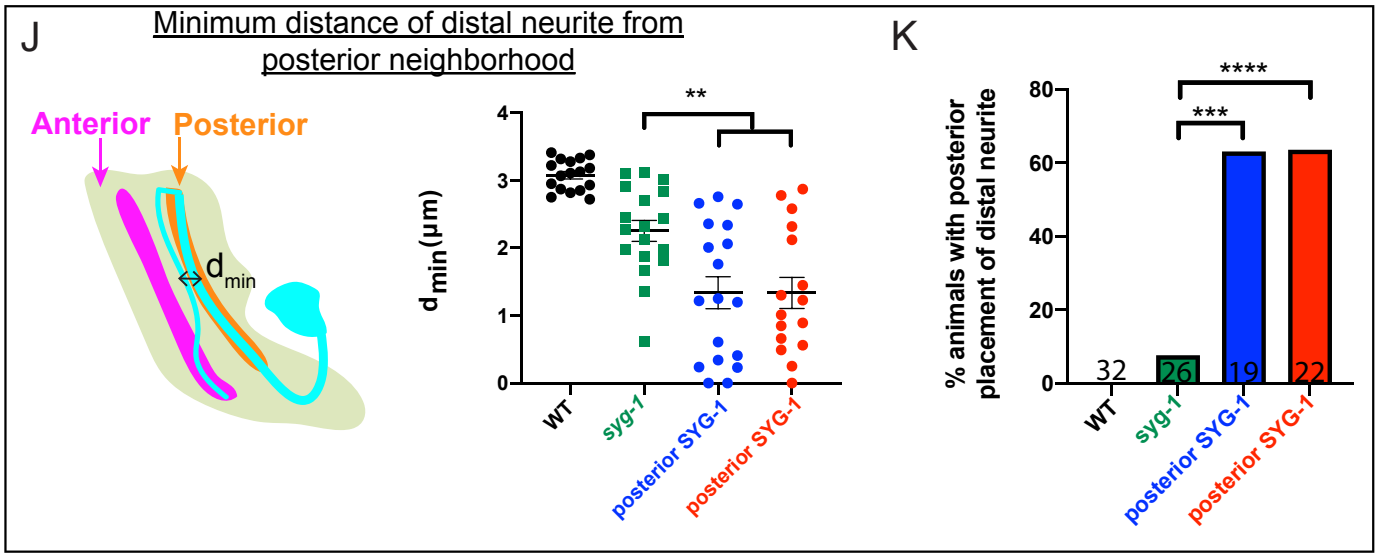

Fig 7

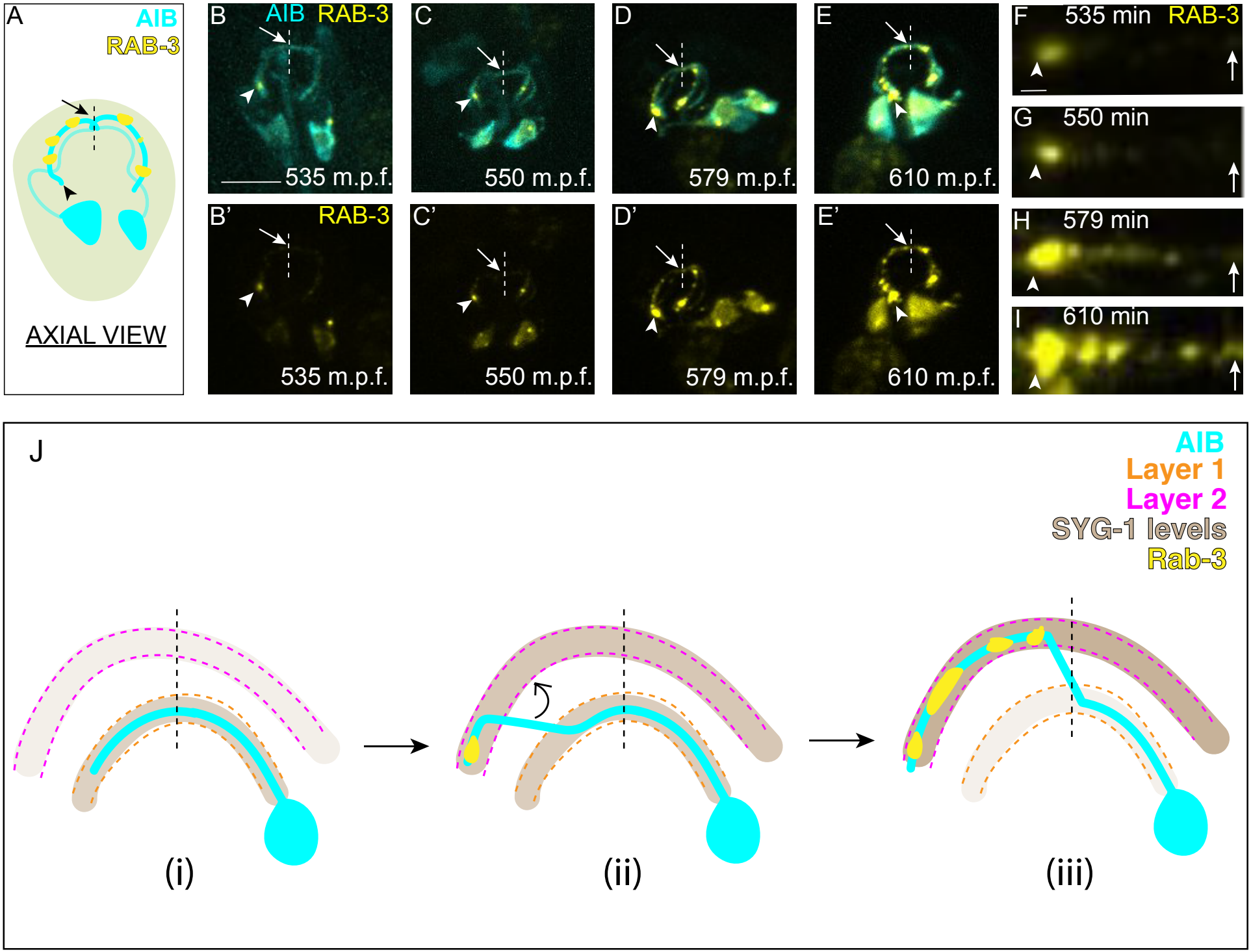
A
AIB
RAB-3
AXIAL VIEW
B AIB RAB-3
535 m.p.f.
C
550 m.p.f.
D
579 m.p.f.
E
610 m.p.f.
B' RAB-3
535 m.p.f.
C'
550 m.p.f.
D'
579 m.p.f.
E'
610 m.p.f.
F 535 min RAB-3
G 550 min
H 579 min
I 610 min
J
AIB
Layer 1
Layer 2
SYG-1 levels
Rab-3
(i)
(ii)
(iii)